machines

MDPI

Review

Review on Melt Electrowriting Modelling and Applications

Hongli Ju [1], Wajira Mirihanage [2], Weiguang Wang [3] and Zekai Murat Kilic [1,*]

[1] Department of Mechanical and Aerospace Engineering, School of Engineering, The University of Manchester, Oxford Road, Manchester M13 9PL, UK; hongli.ju@manchester.ac.uk
[2] Department of Materials, School of Natural Sciences, The University of Manchester, Oxford Road, Manchester M13 9PL, UK; wajira.mirihanage@manchester.ac.uk
[3] Department of Mechanical Engineering, School of Engineering, Faculty of Engineering and Physical Sciences, University of Southampton, University Road, Southampton SO17 1BJ, UK; weiguang.wang@soton.ac.uk
* Correspondence: zekaimurat.kilic@manchester.ac.uk; Tel.: +44-161-529-3407

Abstract

Melt electrowriting (MEW) is an advanced additive manufacturing technology that can produce micro- or nano-scale fibres, achieving accurate fibre deposition, and is suitable for manufacturing high-precision, miniature products. This review introduces the key principles and parameters that influence the performance of melt electrowriting and explores the current mathematical modelling under four stages: (1) heating and extrusion system, (2) formation of the Taylor cone, (3) formation and injection of the melt jet, and (4) deposition of the melt jet. In addition, current applications of melt electrowriting in emerging areas, such as tissue engineering, energy, filtration, and bioengineering, are introduced while discussing its combination with other additive manufacturing technologies. Finally, recent challenges, including production time, cost, and precision are covered, while the future research directions are to improve technology and introduce new materials.

Keywords: melt electrowriting; modelling; tissue engineering; additive manufacturing

Academic Editor: Panagiotis Kyratsis

Received: 28 June 2025
Revised: 12 August 2025
Accepted: 20 August 2025
Published: 25 August 2025

Citation: Ju, H.; Mirihanage, W.; Wang, W.; Kilic, Z.M. Review on Melt Electrowriting Modelling and Applications. *Machines* **2025**, *13*, 763. https://doi.org/10.3390/machines13090763

1. Introduction

Additive manufacturing (AM) is a process that creates physical objects from three-dimensional (3D) digital models by depositing and bonding numerous of thin, continuous layers of material [1]. The most widely used technology is fused filament fabrication (FFF), which is a layer-by-layer 3D printing technology invented by Crump and his company (Stratasys) in 1992 for manufacturing complex geometric parts [2]. In this process, filament material is extruded through a heated nozzle and deposited layer by layer in a semi-solid state onto a partially constructed part [3].

However, the accuracy limitations of FFF have led to increased interest in solution electrospinning (SES), a technique originally developed by Nollet in 1747 [4] and patented by Colley in the early 20th century [5]. In 2001, Bowling et al. successfully demonstrated SES as an advanced manufacturing technology for producing micro- and nano-scale fibres [6]. In 2005, Mikos et al. demonstrated that SES could produce fibres as small as 3 μm in diameter [7]. In 2006, Viswanathan et al. first used SES to produce cellulose nanofibres from a cellulose solution (10 wt%, 1-ethyl-3-methylimidazolium chloride) [8]. Similar to an FFF process, SES uses a polymer solution which is pumped through a nozzle. However, a high voltage is applied between the nozzle and the collector, creating an electrostatic field that generates repulsive forces on the solution, causing it to form a Taylor cone at the tip of the nozzle. When the repulsive force overcomes the surface tension of the solution, the

polymer jet is attracted towards the collector. In the meantime, as the solvent evaporates in SES, the jet undergoes a phenomenon known as "whipping," which causes the jet to thin and random deposition on the collector [9]. The similarity between FFF and SES inspired a study in 2008, in which, for the first time, they were used in combination to facilitate cell seeding by utilising electrospun fibres to fill the pores between each deposited layer [10]. Although whipping may be beneficial for such studies, making SES preferable, whipping would become a challenge if the fibres were to be placed accurately on the collector.

In 2011, Brown, Dalton, and Hutmacher introduced melt electrowriting for the first time [11,12]. This technology uses polymer fibre as the main material, overcomes the "whipping" phenomenon in the SES process, and can produce neatly arranged fibre filaments. In addition, since polymer is used as the material, the time for solvent evaporation is saved, and the problem of solvent residue is also avoided [11]. MEW generally involves two main steps. The first step is similar to FFF technology, where an extrusion system feeds the polymer material into the heating system. When the polymer material is molten, the extrusion system will extrude it through the nozzle. In the second step, as the molten material is deposited, a high voltage is applied between the nozzle and the collector. The voltage exerts an electrostatic attraction on the molten material, producing a Taylor cone. The electrostatic force will pull the material out of the Taylor cone and produce the microfibre, which is then pulled further toward the collector. The applied voltage can stabilise the polymer jet and prevent Plateau–Rayleigh instability [10], which is the phenomenon that breaks a liquid jet into droplets [9].

MEW is a complex manufacturing process with working principles associated with fields such as electronics, thermodynamics, fluid mechanics, and materials science. As shown in Figure 1, an MEW machine typically consists of an extrusion system, a heating system, a print nozzle, and a motion controller. The high-voltage supply is connected to the collector, creating an electric field between the nozzle and the collector [13].

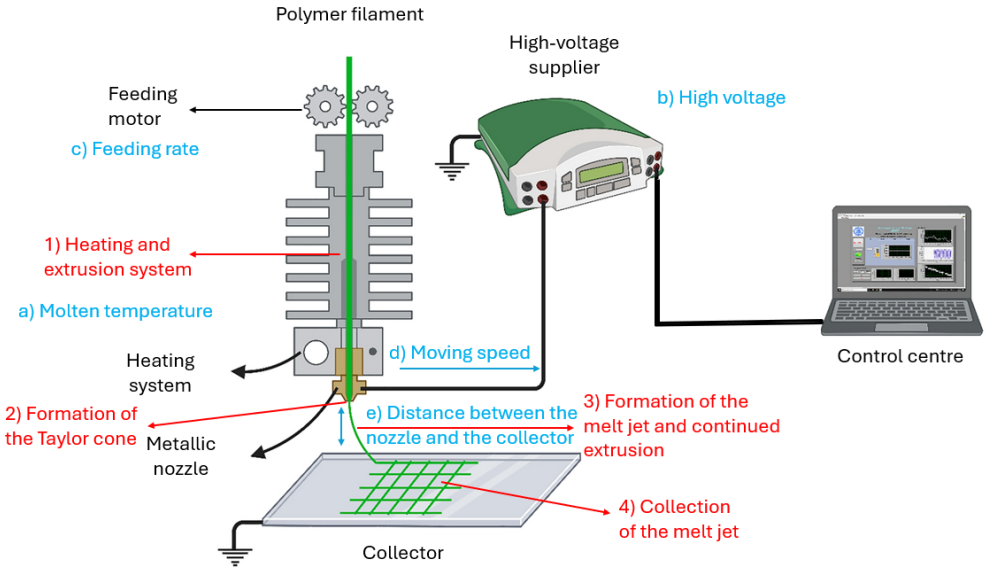

Figure 1. Four stages of the melt electrowriting (MEW) process: (1) heating and extrusion system, (2) formation of Taylor cone, (3) formation of melt jet and continuous extrusion, and (4) collection of melt jet of the MEW process. MEW parameters are labelled as (a) molten temperature, (b) applied voltage, (c) feeding rate, (d) collector/nozzle movement speed, and (e) the distance between the nozzle and collector of MEW. (Figure adapted from [12]).

Over recent decades, extensive research has been conducted on modelling various 3D printing processes; however, MEW has received comparatively limited attention. Therefore, the main motivation of this review is to present the modelling and application aspects

of MEW together, as not carried out earlier in the literature. For the first time, the MEW process is divided into four stages (heating and extrusion system, formation of the Taylor cone, formation and injection of the melt jet, and deposition of the melt jet), and the modelling approach of each stage is discussed in detail and supported by experimental validation. Furthermore, the limitations of existing methodologies are identified, and new directions for future research are proposed to advance the field.

2. Modelling

2.1. Heating and Extrusion System

The American Society for Testing and Materials (ASTM) International generally classifies this method as "material extrusion", which is defined as the selective dispensing of material through a nozzle [14]. The extrusion-based AM technologies can be categorised into three types: (a) filament-based, (b) pressure-based, and (c) screw-assisted extrusion systems. The filament-based extrusion system utilises filament as its raw material, which is pushed into the heating chamber by the drive wheel, where it melts. As the drive wheel continues to press, the molten material is extruded through the nozzle, as shown in Figure 2a. The pressure-based extrusion system is suitable for materials that are inherently fluid (such as molten materials) and materials with low melting points. This system typically utilises a plunger or syringe driven by a motor to promote material flow, as illustrated in Figure 2b. The plunger or syringe can either push the raw material into the heating chamber of the print head or extrude the molten material through the nozzle. In this process, the material does not need to be completely melted, and high pressure allows extrusion at a temperature below the melting point of the material. The screw-based extrusion system is suitable for raw material in small pellet form. The system includes a transport zone (i.e., hopper in Figure 2c), a heater, and an extrusion zone. It works by rotating a screw to feed material into the heating chamber, which melts the material before being extruded through the nozzle [15]. The advantages and disadvantages of each system are given in Table 1 [15,16].

From a review of approximately 40 MEW-related publications from the past decade using the terms "melt electrowriting", "melt electrospinning", and "extrusion system", it was found that more than 85% of MEW equipment utilised filament- and pressure-based extrusion systems, while 10% employed screw-assisted extrusion systems. The remaining 5% of studies did not specify the type of extrusion system used. Therefore, modelling of filament- and pressure-based extrusion systems would cover most of the MEW applications.

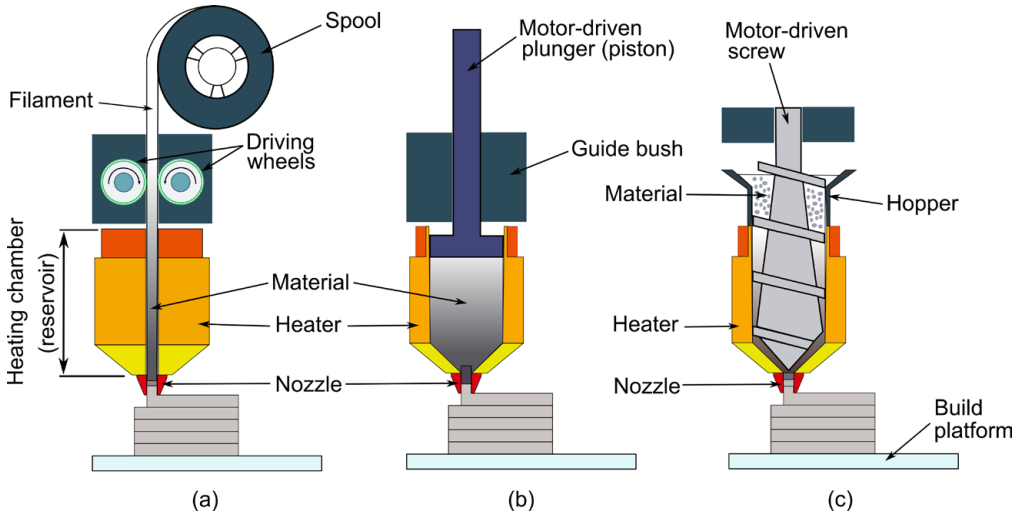

Figure 2. (**a**) Filament-based, (**b**) pressure-based (using plunger, piston, or syringe), and (**c**) screw-assisted extrusion systems. (Figure adapted from [15]).

Table 1. The comparison between the three extrusion systems [15,16].

Extrusion System	Advantages	Disadvantages
Filament-based	Low cost and simple setup Compact print head Reliable on/off control	Limited to filament materials Inconsistent flow at extremes
Pressure-based	Supports wide material types Precise volume control	Pressure lag and poor on/off control Limited reservoir size Sensitive to air compression
Screw-assisted	Processes high-viscosity materials Uses pellets Stable, continuous extrusion	Complex/expensive system Heavy and bulky Cleaning challenges

Although filament- and pressure-based systems have different operating principles, extrusion of the material by either a stepper motor or an air- or fluid-driven plunger, piston, or syringe would exhibit similar thermofluidic behaviour. Hence, the heating and extrusion stage of the MEW process can be explained by a unified, simple model that combines the melt flow model with the downward force-based driving model.

Bellini first investigated the modelling and material flow characteristics in the heater and nozzle in the extrusion process [17]. Based on the experimental results, they developed a model for selecting the shape of the nozzle and simulated the velocity and temperature changes in the material during the experiment. Although the experimental validation was limited to the extrusion of ceramic materials, the findings from the study laid out a foundation for the related literature on processing polymer materials. Later, Ramanath et al. used poly-ε-caprolactone (PCL) as the material and employed an accurate channel model to investigate the changes in velocity, pressure, and temperature of the molten material by varying the filament speed at the inlet, the nozzle shape, and the outlet angle [18]. They found that the material would completely melt at about 35% of the channel length. This result can be used to predict the flow behaviour of other materials. In addition, Monzon et al. evaluated the potential of micro-additive fused deposition (MAFD) through theoretical and experimental research [19]. MAFD uses a smaller diameter nozzle to enhance the accuracy of extrusion. They used Acrylonitrile Butadiene Styrene (ABS) to study the material expansion and cooling during the deposition process by varying the heating temperature and nozzle diameter. They concluded that using a smaller nozzle diameter could significantly reduce the flow rate, by up to 215 times. Ortega et al. used ABS, polylactic acid (PLA), PCL, and polyvinyl alcohol (PVA) as materials to study the suitable working temperature and the shear rate of the MAFD process through modelling [20]. Other relevant models such as the ones in [15] and [21] have also been introduced in the literature.

For the heated extrusion process of MEW, Bellini et al. established a model to simulate the melting and flow of the material [22]. As shown in Figure 3, the model assumes that the filament is at a molten state within the entire heater section, i.e., it ignores the melting process of the filament. Based on [22], Osswald et al. established a new model, as shown in Figure 4 [23]. Among the previous literature, Osswald et al.'s model is the most applicable one to the MEW due to the high similarity in geometric and system parameters; hence, it is introduced in detail below.

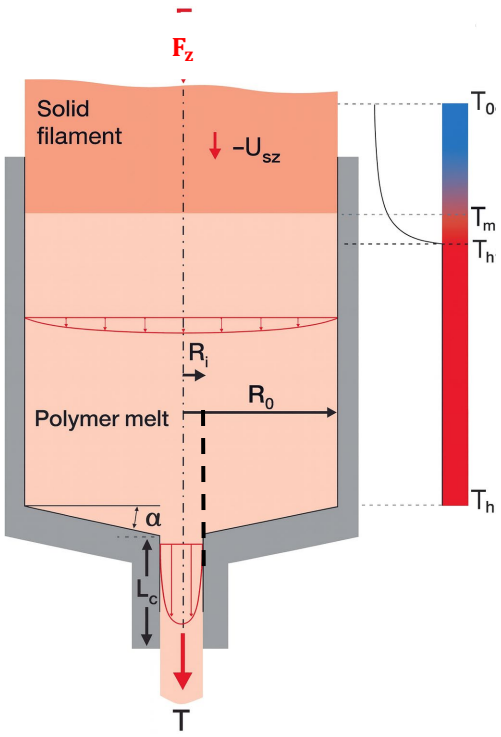

Figure 3. The heating and extrusion model of Bellini et al. [22]. F represents the force applied on the filament, $-U_{sz}$ represents the speed of the filament movement, T_0 is the initial temperature of the filament, T_m is the melting temperature, T_h represents the heater temperature, R_i is the nozzle diameter, R_0 is the diameter of the heater, L_c is the length of the capillary tube, and α is the angle at the nozzle outlet. (Figure from [23]).

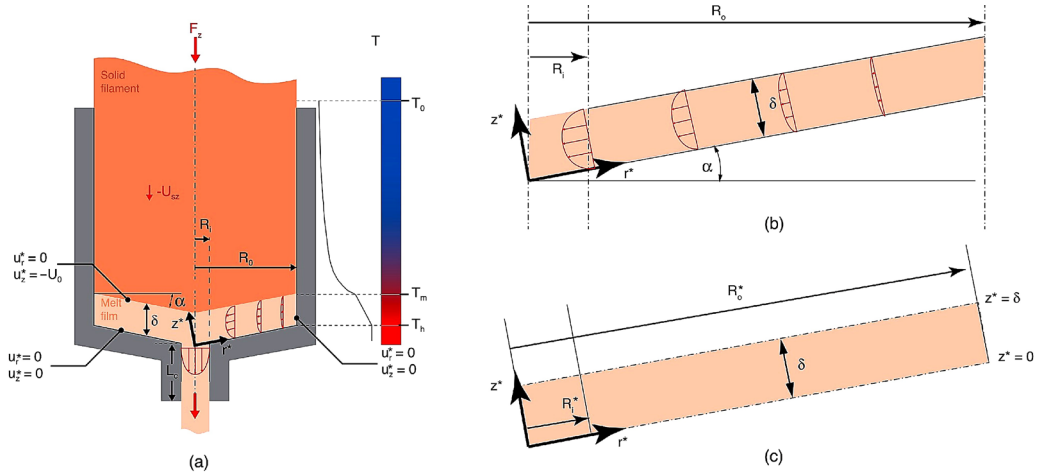

Figure 4. (**a**) The heating and extrusion model established by Osswald et al. (**b**) Detailed display of the film section. (**c**) The model is valid for large R_0/δ ratio, i.e., when the melt film thickness δ is much thinner than the filament diameter. (Figure from [23]).

The mathematical model developed by Osswald et al. provides an analytical approach for simulating the melting and extrusion processes within a fused filament fabrication (FFF) process. The model assumes that a cylindrical filament with an initial radius R_0 is pressed against a heated nozzle surface under a known pressure P. As a result, a thin melt film with thickness δ forms at the filament tip. The melt film, maintained at constant thickness under steady-state conditions, is continuously forced radially inward and extruded through a capillary tube which has a length L_c and radius R_i.

In the model, the temperature of the heater T_h remains constant during the extrusion process. And, the melt–solid interface and filament temperatures are designated as T_m and T_0, respectively. Under the applied force F_z, the filament moves down vertically at a velocity U_{sz}.

To determine the melt film thickness δ and filament velocity U_{sz}, the model can be simplified by assuming zero internal nozzle angle (i.e., $\alpha = 0$). Then, for the fluid viscosity μ_f, the momentum balance equation in the melt film can be written as

$$0 = -\frac{dp}{dr^*} + \mu_f \frac{d^2 {u_r}^*}{dz^{*2}} \tag{1}$$

where p is the pressure applied by the force F_z. r^* and z^* are the transformed radial and axial coordinates, respectively. u_r^* is the radial velocity in the melt film.

The capillary entrance pressure follows the Hagen–Poiseuille relationship:

$$p_i = \frac{8\mu_c Q L_c}{\pi {R_i}^4} \tag{2}$$

where μ_c is the melt viscosity within the capillary, Q is the volumetric flow rate, L_c is the capillary length, and R_i is the radius of the capillary.

The volumetric flow rate defined by the mass balance is

$$Q = \pi {R_o}^2 (-U_{sz}) \tag{3}$$

Thus, the pressure at the capillary entrance becomes

$$p_i = \frac{8\mu_c {R_o}^2 (-U_{sz}) L_c}{{R_i}^4} \tag{4}$$

Then, the axial force balance, which relates the applied force F_z to velocities and melt film parameters, is expressed as

$$F_z = \left(\frac{6\pi\mu_f \mu(-U_0) R_0}{\cos(\alpha)} \frac{{R_0}^3}{\delta^3}\right)\left[In\left(\frac{R_i}{R_o}\right) + \frac{3}{4} + \frac{1}{4}\left(\frac{R_i}{R_o}\right)^4 - \left(\frac{R_i}{R_o}\right)^2\right] - 8\pi\mu_c(-U_{sz}\hat{\rho}) L_c \left(\frac{R_o}{R_i}\right)^2 \tag{5}$$

The melt film thickness δ is determined from the energy balance (Stefan condition), where the thermal conductivity of the molten material k_m plays a crucial role:

$$\delta = \frac{k_m(T_h - T_m)}{\rho_s(-U_{sz})[\lambda + C_s(T_m - T_0)]} \tag{6}$$

where C_s and ρ_s are the specific heat capacity and density of the filament (solid) material. And, the latent heat of fusion λ represents the energy required for the filament to transition from solid to molten state.

Finally, the filament velocity (U_{sz}), which determines the melting and extrusion speed, can be computed by numerically solving the following force–velocity equation:

$$\left(\frac{(-U_{sz})\frac{6\pi\mu_f\hat{\rho}{R_0}^4}{cos(\alpha)}\left[In\left(\frac{R_i}{R_0}\right) + \frac{3}{4} + \frac{1}{4}\left(\frac{R_i}{R_0}\right)^4 - \left(\frac{R_i}{R_0}\right)^2\right]}{F_z - \left(-8\pi\mu_c\hat{\rho}L_c\left(\frac{R_0}{R_i}\right)^2\right)(-U_{sz})}\right)^{\frac{1}{3}} = \frac{k_m(T_h - T_m)}{\rho_s(-U_{sz})[\lambda + C_s(T_m - T_0)]} \tag{7}$$

Compared to earlier models, Osswald et al.'s analytical model uniquely integrates thermal and mechanical behaviour of the extrusion process. Thus, it can explain the increased filament velocity with increased force by the reduced melt film thickness. Furthermore,

their model's accuracy and applicability have been experimentally validated by the setup shown in Figure 5. A comparative table with different models of heating and extrusion system is shown in Table 2.

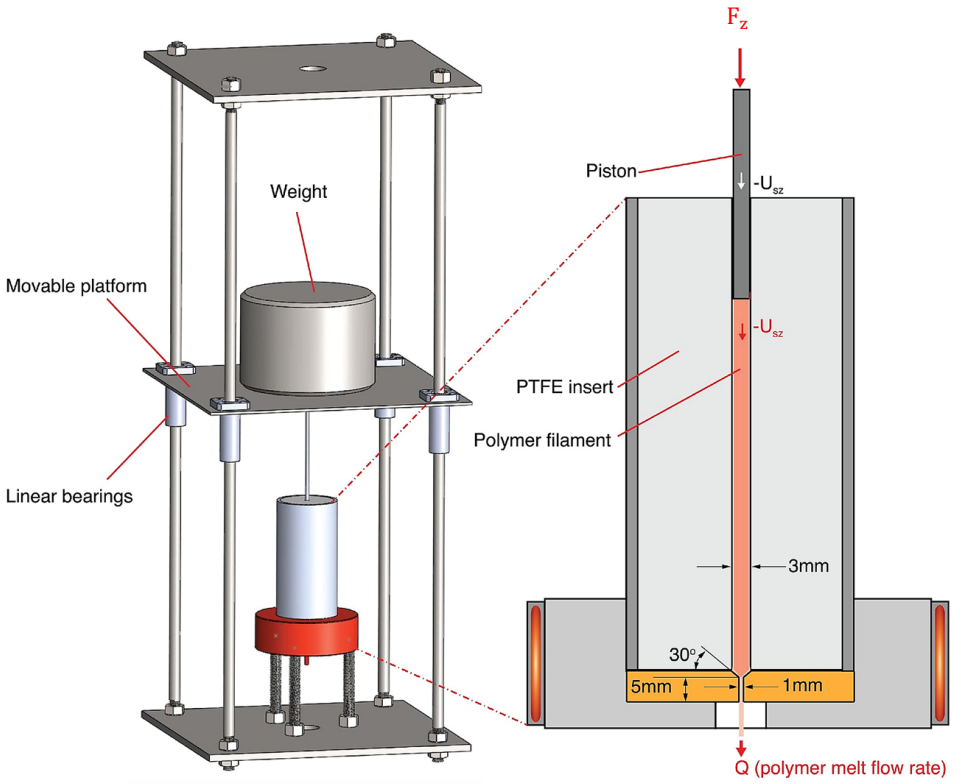

Figure 5. The setup of the experiment device. Vertical red coloured arrows indicate the direction of the force F_z and the flow direction of the molten material. (Figure is adapted from [23]).

Table 2. Comparative summary of heating and extrusion system models.

Model Authors	Assumptions	Applications	Limitations
Bellini et al. [17,22]	- Material is already molten upon entering the heater - Ignores melting process inside the heater	- Simulates velocity and temperature profiles to optimise nozzle geometry	- Does not consider solid-to-liquid phase transition - Not validated specifically for polymers
Ramanath et al. [18]	- Accurate channel geometry - Varies filament speed, nozzle shape, and outlet angle	- Predicts molten material's flow behaviour (velocity, pressure, and temperature)	- Limited to PCL - Validation is restricted to a single polymer type
Monzon et al. [19]	- Investigates smaller nozzle diameters and temperature variations	- Enhanced accuracy and resolution of extrusion using smaller nozzles - Analysis of material expansion and cooling effects	- Specific to ABS - Reduced flow rate may avoid practical extrusion rates
Ortega et al. [20]	- Evaluates optimal temperature and shear rate - Applies to multiple polymer types	- Optimisation of processing conditions for various materials in MAFD	- Increased model complexity with multiple polymers - Simplified shear dynamics

Table 2. *Cont.*

Model Authors	Assumptions	Applications	Limitations
Osswald et al. [15,21]	- Cylindrical filament pressed onto heated nozzle forming melt film at constant thickness - Steady-state extrusion under constant heater temperature - Considers latent heat of fusion, melt–solid interface, and initial filament temperature	- Analytical prediction of melting and extrusion behaviour for MEW and FFF processes	- Assumes ideal steady-state conditions - Does not fully capture transient behaviour or variations

2.2. Formation of the Taylor Cone

In 1964, Sir G. I. Taylor observed that under the action of a strong electric field at the tip of a capillary, a water droplet forms a conical structure, which then develops into a short jet before forming an electrospray [24]. The conical structure, which is known as a Taylor cone, is formed when a small amount of conductive liquid is exposed to a strong electric field. In 1969, Taylor employed a double-plate experimental apparatus to investigate the deformation criteria of extruded molten materials as they transition from a sphere to a cone. When the molten material at the nozzle tip is spherical, the electrostatic force, fluid dynamics, surface tension, and the gravity of the sphere are in equilibrium. As the electric field strength increases and gravity continues to act, the cone becomes unstable, and a very thin stream of liquid is ejected from the top of the cone [25]. In this process, it is assumed that the fluid is a perfect dielectric, that is, there is no free charge and the conductivity is zero. The deformation of the droplet or jet is only due to the polarisation of the dielectric. Figure 6 illustrates the progression from Taylor cone formation to jet formation, ejection, and subsequent events [26].

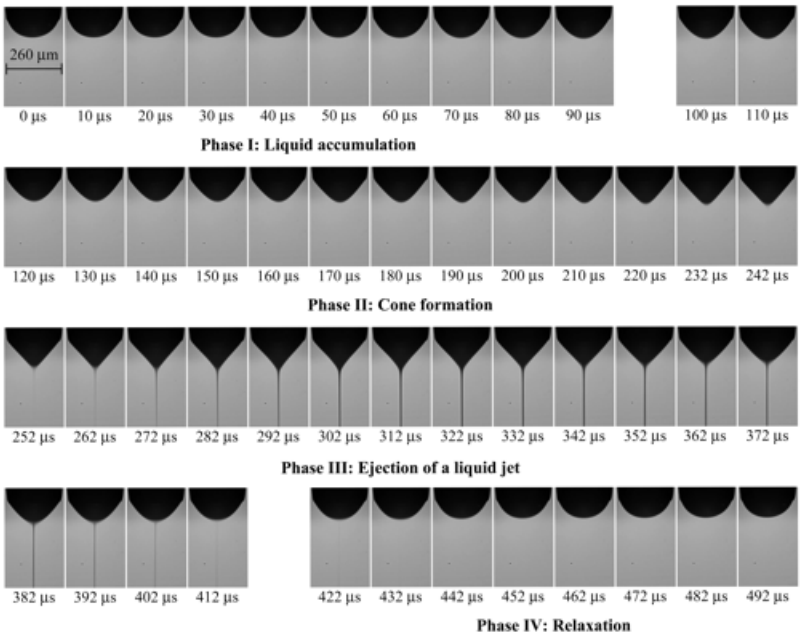

Figure 6. The process from Taylor cone formation to jet formation and ejection to the end. (Figure is taken from [26]).

To accurately predict the formation of cones and jets, Taylor and Melcher devised the Taylor–Melcher leaky dielectric model, which assumes that the fluid is a leaky dielectric,

i.e., its conductivity is small but not negligible [27]. The electric field induces the accumulation of free charges at the liquid–air interface, generating electric stress in both the normal and tangential directions. Figure 7 shows the distribution of forces acting within the liquid cone jet according to the leaky dielectric model. At the liquid–air interface, normal electric stress is balanced by surface tension, while viscous flow counterbalances tangential components of electric field stress [28].

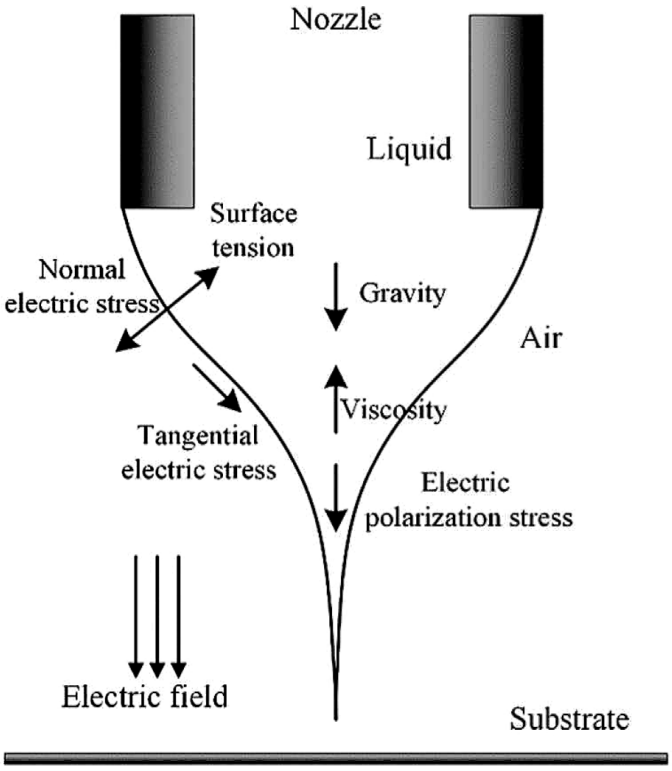

Figure 7. Distribution of active forces on the liquid cone jet. (Figure is adapted from [28]).

During the process, the motion can be described by the following equations of continuity and conservation of momentum:

$$\nabla \cdot \vec{v} = 0 \tag{8}$$

$$\rho \frac{d\vec{v}}{dt} = -\nabla P + \eta \nabla^2 v + \vec{f_e} + \rho \vec{g} \tag{9}$$

where ∇ is the divergence, P is the pressure, t is the time, $\vec{v}$ is the fluid velocity, η is the viscosity, ρ is the density and $\vec{f_e}$ is electromechanical force:

$$\vec{f_e} = q_e \vec{E} \tag{10}$$

where q_e is the charge density and $\vec{E}$ is the electric field. They are formulated as

$$q_e = \varepsilon \nabla \cdot \vec{E} \tag{11}$$

$$E = -\nabla \phi \tag{12}$$

where ε is the relative dielectric constant of liquid and ϕ is the electric potential. According to these two equations, the electromechanical force can be expressed as

$$\vec{f_e} = -\varepsilon \nabla^2 \phi \cdot \vec{E} \tag{13}$$

The charge conservation is represented as follows:

$$\frac{\partial q}{\partial t} + \nabla \cdot \vec{J} = 0 \tag{14}$$

where the current density $\vec{J}$ is expressed as

$$\vec{J} = q\vec{v} + \sigma \vec{E} \tag{15}$$

where σ is the electrical conductivity of the liquid.

In 1997, Gañán-Calvo et al. proposed a mathematical model to describe the physical process of liquid electrostatic spraying in the cone jet mode [29]. The model identified the relationship between current, flow rate, and droplet size in high-conductivity, high-viscosity liquids and low-conductivity, low-viscosity liquids. In 1999, Barrero et al. improved this model by introducing the Reynolds coefficient (Re) and derived the quantitative relationship between flow rate, shear stress, surface electric field, and fluid parameters. They found that conductivity significantly influences the shear stress generated by the electric field on the Taylor cone surface and gave a practical formula that can be used for experiments and predictions [30]. Although certain general principles can be derived from theoretical modelling under simplified conditions through theoretical modelling, it is still quite challenging to study the behaviour mechanism of droplet generation.

With advances in numerical methods, including the finite element method (FEM) and finite volume method (FVM), researchers began to simulate the formation of cone jets by developing computational solvers or using commercial software based on the Taylor–Melcher leaky dielectric model. In 2003, Yan et al. first established a two-dimensional model of the conical jet's morphology using numerical simulations [31]. In 2006, Lastow and Balachandran also successfully simulated the morphology of a conical jet using Ansys CFX [32]. During the simulation process, a corresponding user-defined function (UDF) was introduced to enhance simulation accuracy. However, due to the simplicity of the model, it could not accurately capture the phenomenon of jet breakup. In 2012, Wu et al. simulated the formation and breakup of a conical jet and investigated the effect of nozzle design parameters on jetting behaviour [33].

In 2019, Pan et al. established a numerical simulation model to study the dynamic behaviour of droplet generation during electrohydrodynamic jet (E-jet) printing [28]. The model simulates four stages: Taylor cone formation, jet formation, jet breakage, and droplet retraction. The effects of applied voltage, liquid flow, rate and nozzle diameter on droplet size, electric field distribution, and deposition accuracy were studied. The key design constraints for droplet generation were proposed: (1) the starting voltage must be higher than the critical value, and the flow rate, and (2) nozzle size must match the liquid properties to ensure jet stability. In 2020, Sachin et al. established a similar model based on the phase field method to simulate the entire process from nozzle outlet to droplet deposition [34]. The model investigated the effects of conductivity, dielectric constant, viscosity, surface tension of the liquid and the applied electric field, flow rate, and nozzle diameter on the jetting behaviour and summarised the electric field distribution, jet diameter, and droplet generation laws. The model also studied the role of current components (conduction current and convection current) in droplet generation. In 2023, Cândido and Páscoa proposed a numerical simulation model based on the volume-of-fluid (VoF) method to investigate the physical mechanism of liquid jet generation and stability during electrohydrodynamic (EHD) jetting [35].

A comparative table about models of formation of the Taylor cone is shown in Table 3. Current models effectively simulate the entire process from Taylor cone formation through jet deposition, considering the influence of most physical and experimental factors. However, existing models insufficiently account for complex fluid morphologies and environmental conditions. Therefore, future research should focus on extending the model to three-dimensional asymmetric conditions and incorporating the characteristics of complex fluids and the influence of environmental factors.

Table 3. Comparative overview of Taylor cone formation models.

Model Authors	Assumptions	Applications	Limitations
Taylor (1964, 1969) [24,25]	- Fluid treated as a perfect dielectric (zero conductivity and no free charge) - Deformation due to polarisation only	- Fundamental studies on droplet deformation and jet formation under electric fields	- Ignores conductivity - Oversimplified for practical use
Melcher and Taylor (1969) [27]	- Leaky dielectric model with finite conductivity - Free charge accumulation induces normal and tangential electric stresses	- Analysis of Taylor cone and jet formation in fluids with finite conductivity	- Does not accurately represent highly conductive materials - Simplified physical conditions
Gañán-Calvo et al. (1997) [29]	- Correlates current, flow rate, and droplet size - Considers various conductivity and viscosity	- Quantitative predictions for electrospray processes - Basis for practical design	- Limited to steady-state conditions - Simplified physical conditions
Barrero et al. (1999) [30]	- Includes Reynolds number (Re) - Conductivity significantly affects shear stress	- Practical formula for predicting jet behaviour and optimising spray parameters	- Assumes simplified physical conditions - Limited generalisability due to specific fluid constraints
Yan et al. (2003) [31]	- 2D FEM/FVM numerical simulations - Based on Taylor–Melcher model	- Numerical visualisation of jet morphology and flow	- Cannot fully capture jet breakup - Simplified model
Lastow and Balachandran (2006) [32]	- Improved accuracy by user-defined functions - Based on Taylor–Melcher model	- Enhanced numerical simulation of conical jet formation using commercial software	- Simplified assumptions - Incomplete modelling of jet breakup dynamics
Wu et al. (2012) [33]	- Examines nozzle design effects on jetting behaviour - Simulates jet breakup phenomena	- Detailed analysis of jet breakup dynamics and nozzle design influence	- High computational demand - May oversimplify complex interactions
Pan et al. (2019) [28]	- Simulates Taylor cone and jet formation, breakup, and droplet retraction - Studies effects of voltage, flow rate, and nozzle radius	- Optimisation of printing parameters and understanding jet dynamics for E-jet printing	- Numerical complexity - Sensitive to parameter variations

Table 3. *Cont.*

Model Authors	Assumptions	Applications	Limitations
Sachin et al. (2020) [34]	- Considers conductivity, dielectric constant, viscosity, surface tension, and electric field - Detailed analysis of electric field distribution, jet diameter, and droplet generation - Studies conduction and convection currents	- Comprehensive simulation of E-jet processes from nozzle to deposition - Practical insights into parameter effects	- Complex simulation requirements - Significant computational resources needed
Cândido and Páscoa (2023) [35]	- Uses VoF method to study jet generation and stability - Detailed investigation of physical mechanisms in EHD jetting processes	- Accurate modelling of EHD jetting processes - Improved understanding of physical mechanisms	- Computationally demanding - Accuracy depends on mesh resolution

2.3. Melt Jet Formation and Continuous Extrusion

In MEW, the formation and extrusion of the melt jet is influenced by several factors, such as temperature; applied electric field; as well as the melt viscosity, which closely depends on the type of the fluid. Newtonian fluids (e.g., water) maintain constant viscosity under shear force, whereas non-Newtonian fluids exhibit varying behaviours depending on the shear rate [36]. Molten polymer is a typical example of a non-Newtonian fluid, which is more challenging to model. Therefore, this section explains the complex dynamics involved in melt jet formation and the extrusion stage of MEW.

Spivak and Dzenis first proposed a steady-state jet model for the SES process [37]. Later, Hohman et al. established a model to analyse the change in jet stability during the SES process with the increased intensity of the electric field [38,39]. In their model, they regarded the polymer solution as a Newtonian fluid. Based on Hohman et al.'s model, Feng et al. introduced a charged non-Newtonian jet model, which is a more accurate representation of the process in SES. To simulate the SES process, they later combined it with Giesekus's model [40], which is a nonlinear constitutive equation to describe the flow behaviour of a polymer fluid [41]. Carroll et al. developed a new model based on Feng et al.'s model by combining the steady-state conservation equations for mass, charge and momentum with the electric field equation derived from electrostatic principles [42].

Based on Carroll et al.'s model [42], Zhmayev et al. modelled processing of polylactic acid (PLA) material via MEW [43]. Their approach, however, focused exclusively on fibre formation, without accounting for the motion of the nozzle. The model is formulated using steady-state equations.

The continuity equation for the melt jet is given by

$$\pi R^2 v = Q \tag{16}$$

where R is the radius of the jet, v is the flow speed, and Q is the volumetric flow rate.

The momentum balance is expressed as

$$\rho v v' = \rho g + \frac{F_T'}{\pi R^2} + \frac{\gamma R'}{R^2} + \frac{\sigma \sigma'}{\varepsilon_0} + (\varepsilon - \varepsilon_0) E_t E_t' + \frac{2\sigma E_t}{R} \tag{17}$$

where ρ is the fluid density; g is gravitational acceleration; $F_T = \pi R^2(\tau_{zz} - \tau_{rr})$ represents the tensile force (within the jet) derived from fluid stresses; γ is the surface tension; σ

is the charge density; and $\varepsilon, \varepsilon_0$ are the dielectric constants of the jet and the ambient air, respectively. E_t is the tangential component of the electric field at the jet surface. The primes, e.g., v', $R\prime$, and E_t', indicate derivatives with respect to the axial coordinate z.

The charge on the melt jet is determined by

$$2\pi Rv\sigma = I \text{ where } \sigma_0 = \varepsilon_0 E_n(0) \approx \varepsilon_0 E(0) \tag{18}$$

with I being the current.

The electric field is approximated by

$$E(z) \approx E_\infty(z) = \frac{2V}{(R_0 + 2z - z^2/d)In(1 + 4d/R_0)'} \text{ and } E_t(z) = \frac{E(z)}{\sqrt{1 + (R')^2}} \tag{19}$$

where V is the applied voltage between the nozzle and collector, E_∞ is the applied external electric field, d is the distance between the nozzle and collector, and R_0 is the nozzle radius. The model can predict fibre diameters by varying parameters such as nozzle temperature, feed rate of the molten polymer, and applied voltage.

Zhmayev et al. also experimentally validated the accuracy of their model. They first heated the PLA material to 200 °C for 30 min and then loaded the molten material into the MEW machine. They designed three sets of experiments; each was for varying another parameter: (1) nozzle temperature, (2) feed rate of the molten polymer, and (3) the distance between the nozzle and collector. These variations resulted in the production of fibres with different diameters. Subsequent measurements of the fibre diameters showed good agreement with the model's predictions. Figure 8a–c show comparative results illustrating the influence of these parameters.

Building on their earlier work, Zhmayev et al. introduced a comprehensive model to describe the stable jet region in crystalline polymer melt electrospinning [44]. This model integrates Ziabicki's classical flow-induced crystallisation (FIC) framework [45] with a non-isothermal melt electrospinning approach. Experimental validation was carried out using nylon-6 as the working material. The proposed model demonstrated consistency with Ziabicki's simulation results under both isothermal and non-isothermal conditions. Notably, in contrast to the traditional FIC model, the new formulation provides additional microstructural information, including grain number density and average grain size.

Mayadeo et al. further investigated the impact of introducing a heat source between the nozzle and the collector on fibre diameter through both modelling and experimental studies [46]. They developed an extended model based on Zhmayev et al.'s model and found that the application of heat led to a reduction in fibre diameter, aligning well with experimental observations.

Currently, Zhmayev et al.'s model stands as the most widely cited in modelling electrospun fibres, with over 100 publications referencing it. However, one limitation of the model is its assumption of negligible electrical conductivity in the molten polymer. As a result, it ignores the contribution of electrical currents carried by the polymer and the axial conduction of current under an applied electric field. With the anticipated shift toward using highly conductive materials in future MEW applications, it will be essential for future models to incorporate these electrical effects.

A comparative overview of melt jet formation and continuous extrusion models is presented in Table 4.

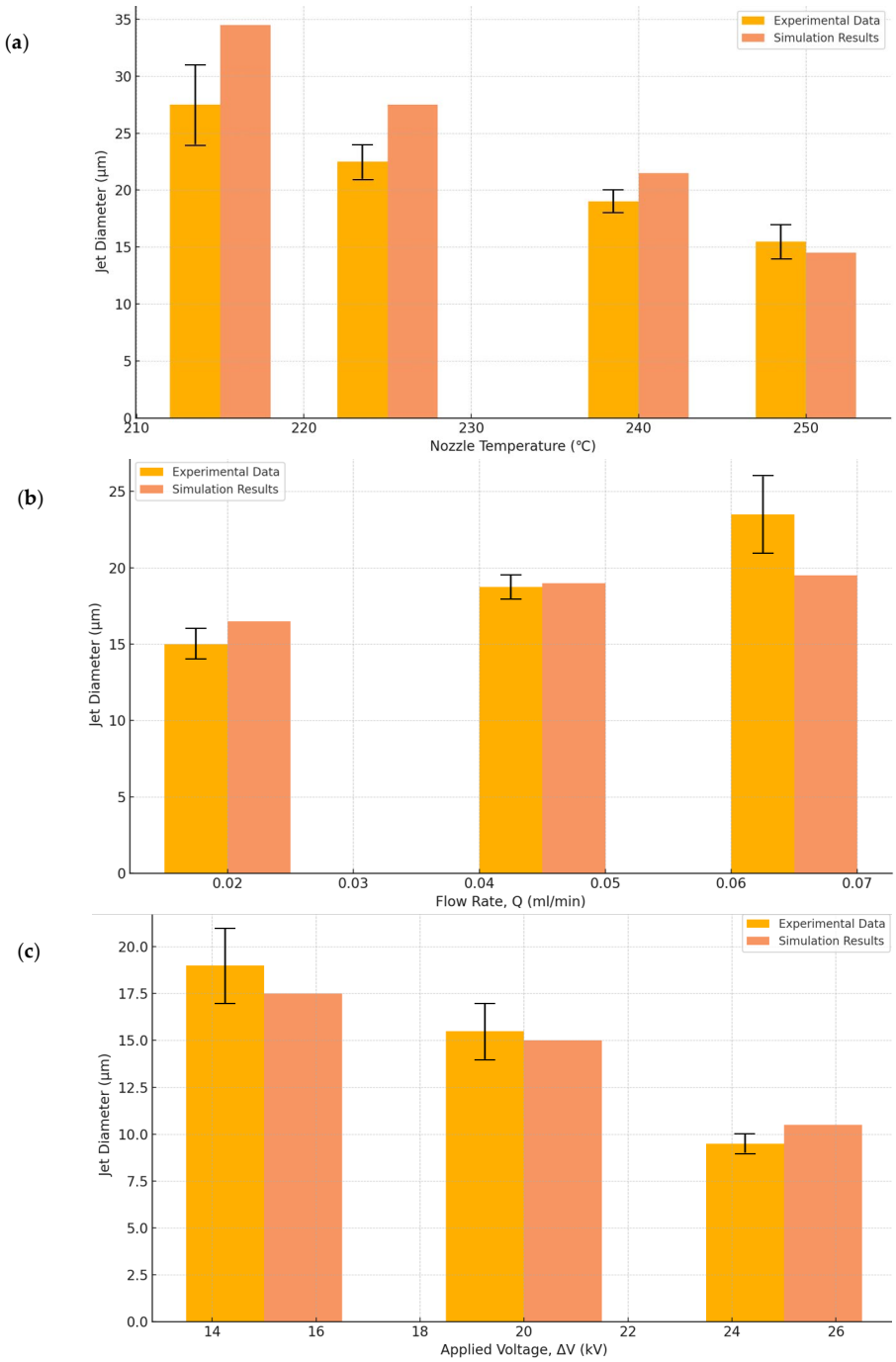

Figure 8. (**a**) Effect of nozzle temperature on fibre diameter, (**b**) effect of feeding rate on fibre diameter, (**c**) effect of applied voltage on fibre diameter (data adapted from [43]).

Table 4. Comparative summary of key models in melt jet formation and continuous extrusion literature.

Model Authors	Assumptions	Applications	Limitations
Spivak and Dzenis [37]	- Assumes steady-state jet flow - Simplified fluid dynamics	- Fundamental model for steady-state jet behaviour in solution electrospinning (SES)	- Limited to steady-state conditions - Not applicable to varying field strengths or unsteady processes

Table 4. *Cont.*

Model Authors	Assumptions	Applications	Limitations
Hohman et al. [38,39]	- Treats polymer solution as Newtonian fluid - Studies jet instability under increasing electric field	- Investigates instability mechanisms in electrospinning jets	- Inaccurate for non-Newtonian fluids, e.g., molten polymers
Feng et al. [40,41]	- Uses Giesekus model for non-Newtonian behaviour - Includes charge effects and viscoelasticity	- More realistic modelling of polymer jets - Improved accuracy over Newtonian models	- Simplified charge and field distributions - Sensitive to parameter selection
Carroll et al. [42]	- Based on Feng et al.'s model - Integrates steady-state equations for mass, charge, momentum, and electric field	- Experimentally validated for accurate SES simulations	- Complex model equations - Computationally expensive
Zhmayev et al. [43]	- Based on Carroll et al.'s model - Ignores nozzle movement - Focusses on fibre formation	- Predicts fibre diameter based on temperature, feed rate, and nozzle-to-collector distance	- Excludes nozzle dynamics - Limited to fibre characteristics
Zhmayev et al. [44]	- Combines Ziabicki's fibre internal crystallisation (FIC) model with non-isothermal conditions	- Simulates crystalline fibre formation - Enables microstructural predictions	- Applicable only to crystalline polymers - Requires detailed thermal and material data
Mayadeo et al. [46]	- Extends Zhmayev et al.'s model - Introduces external heating between nozzle and collector - Experimentally validated	- Demonstrates heat-assisted control of fibre diameter in MEW	- Limited to systems with external heating infrastructure

2.4. Collection of the Melt Jet

In the MEW process, fibre collection is the most critical and complex stage. Several process parameters influence this stage: (1) applied voltage determines the electric field strength, directly affecting the tensile force exerted on the fibre; (2) temperature influences the viscosity of the molten polymer; (3) stand-off distance between the nozzle and collector impacts fibre cooling rate and deposition uniformity; (4) printing speed determines the deposition pattern and fibre diameter; (5) environmental conditions, such as ambient temperature and humidity, affect fibre toughness and deposition accuracy; and (6) collector properties, including conductivity and surface roughness, also play a significant role.

Accurately modelling the MEW process while accounting for all these variables remains a challenge. Fortunately, prior research has made notable progress in this area.

In 2020, Hrynevich et al. introduced a geometric model to predict fibre deposition paths during MEW [47]. This model addresses deviations between the actual and programmed deposition trajectories by integrating nozzle motion, collector plate speed, and geometric calculation of jet lag. It assumes the nozzle speed exceeds the critical transla-

tion speed (CTS) and ignores complex factors such as fibre crossing, charge distribution, and environmental variability. Despite these simplifications, the model achieves high prediction accuracy in single-layer printing, with deviations under 70 µm—ten times more precise than predictions based solely on G-code. However, its applicability is limited to flat, single-layer prints and requires extension to multi-layer or 3D structures.

In 2022, Cao et al. developed a mathematical model to analyse the dynamic relationship between nozzle position and fibre contact point during MEW [48,49]. This model enables the prediction and control of path deviations, enhancing printing accuracy. Experimental validation was performed using straight lines and steady-state curves. However, the model builds directly on Hrynevich et al.'s geometric model [47] and does not incorporate physical complexities such as rheological behaviour of the material (deformation or flow under external force or stress) or charge effects, limiting its use in multi-layer and high-speed printing scenarios.

Beyond these geometric models, Ko et al. proposed a comprehensive mathematical model in 2014 to simulate the entire MEW process from Taylor cone formation to fibre collection [50]. This model treats the molten polymer as a viscoelastic fluid with constant density, viscosity, surface tension, and dielectric constant, assuming a uniform temperature field. During geometric modelling, the melt at the nozzle outlet is simplified as a truncated sphere. As shown in Figure 9, the formation of a truncated cone (i.e., Taylor cone) and a cylindrical jet is simulated under an applied electric field.

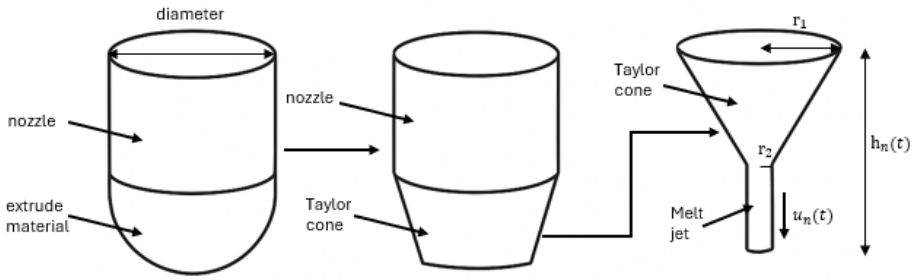

Figure 9. The shape of the Taylor cone.

The model is based on volume conservation and derives the relationship between nozzle radius r_1 and jet radius r_2:

$$r_2(t) = \frac{-h_1(t)\pi r_1 \pm \sqrt{3\pi}\sqrt{-4(h_1(t) - 3h_2(t))Qt - h_1(t)(h_1(t) - 4h_2(t))\pi r_1^2}}{2(h_1(t) - 3h_2(t)\pi)} \quad (20)$$

where Q is the feed rate of the molten material. Initially, the droplet height h_0 equals the nozzle radius. After applying an electrical field, the polymer melt moves toward the collector and the jet height changes over time. The Taylor cone height h_1 and jet height h_2 are given by

$$h_n(t) = h_{n-1} + \int_0^t u_n(t)dt \quad (21)$$

where n = 1,2 and the jet velocity $u_n(t)$ at time t is

$$u_n(t) = u_{n-1} + \int_0^t \frac{\sum F}{m} dt \quad (22)$$

Here, n = 1 corresponds to the Taylor cone velocity and n = 2 to the jet velocity. $\sum F$ represents the total force acting on the molten polymer droplet.

The straight jet in the MEW process is affected by several forces, including surface tension F_s, electric stress force F_v, gravity F_g, and electrostatic force F_e. These forces are described within the framework of the Taylor–Melcher leaky dielectric model [28].

During the modelling of the deposition trajectory, the path was estimated based on the fibre diameter and fibre velocity. The initial test involved printing a circular loop. Given that the distance between the nozzle and collector is constant, the deposition path was simplified into a two-dimensional model, as illustrated in Figure 10. Then, the position of the fibre on the collector is defined by the following expression:

$$P_s(x,y) = \int V_A + \int V_L = \begin{bmatrix} R_T cos(\omega t) \\ R_T sin(\omega t) \end{bmatrix} + \begin{bmatrix} V_L t \\ 0 \end{bmatrix} \tag{23}$$

where V_A is the angular velocity component, V_L is the linear velocity component, R_T is the radius of the circular loop, and $\omega = \frac{u}{R_T}$ is the angular velocity derived from the nozzle speed u.

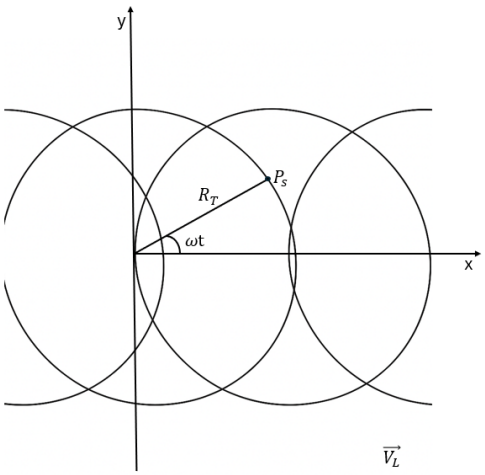

Figure 10. Circular loop pattern and corresponding position trajectory.

To simplify the modelling process, several complex factors were excluded, including the effects of the external environment, chemical reactions within the solution, magnetic field effects in the electric field, non-Newtonian fluid behaviour, and multiphase flow dynamics. The proposed mathematical model explains the entire MEW process from melt extrusion and Taylor cone formation to fibre deposition. For the first time, a relationship was established between input parameters (such as nozzle diameter, applied voltage, and temperature) and output indicators (such as fibre diameter and deposition location), providing a better understanding of MEW for applications in tissue engineering and customised scaffold fabrication.

A comparative overview of fibre collection models is presented in Table 5.

Current MEW modelling has made significant progress by integrating disciplines such as fluid mechanics, electrodynamics, and materials science, leading to improved process prediction accuracy. However, most existing models rely on simplified assumptions, overlooking the complexities of non-Newtonian fluids, multiphase flow behaviour, and dynamic environmental conditions. Their applicability is generally confined to single-layer structures or basic geometries. Future research should aim to develop more comprehensive models that incorporate complex fluid properties and environmental factors, extend applicability to multi-layer and intricate structures, and integrate advanced numerical techniques (such as machine learning) to support the evolving demands of MEW in high-precision and complex biomanufacturing.

Table 5. Comparative analysis of fibre collection models.

Model Authors	Assumptions	Applications	Limitations
Hrynevich et al. (2020) [47]	- Assumes nozzle speed exceeds CTS - Uses geometric estimation of jet lag - Ignores fibre crossing, charge effects, and environmental factors - Designed for flat, single-layer printing	- Accurately predicts fibre deposition path in single-layer MEW (error < 70 μm)	- Not suitable for multi-layer or 3D structures - Does not consider material rheology or ambient conditions
Cao et al. (2022) [48,49]	- Based on Hrynevich et al.'s model - Introduces dynamic interaction between nozzle and fibre contact point - Does not consider rheological and electrostatic effects	- Improves printing accuracy by compensating for path deviation in linear and curved paths.	- Limited to simple geometries - Inaccurate for high-speed or multi-layer printing due to physical simplifications
Ko et al. (2014) [50]	- Assumes viscoelastic polymer with constant properties (density, viscosity, surface tension, and dielectric constant) - Uniform temperature with no gradients - Excludes environmental effects, magnetic fields, and complex fluid behaviours	- Provides a complete MEW framework linking input (e.g. voltage and nozzle radius) to outputs (e.g., fibre diameter and deposition location)	- Highly idealised - Does not account for dynamic temperature changes or real-life environmental influences

3. MEW Applications

Melt electrowriting (MEW) serves as a bridge between traditional electrospinning and extrusion-based 3D printing, enabling the fabrication of complex microscale geometries. This is achieved through a layer-by-layer fabrication process combined with precise fibre control under an electrostatic field, without the use of chemical solvents, which may be detrimental to human and environmental health. These distinctive advantages set MEW apart from other microfabrication techniques, making it particularly suitable for applications demanding structural precision, biocompatibility, and design flexibility. Consequently, MEW has attracted increasing attention across diverse fields, including energy storage, filtration and separation, microfluidics, and bioengineering. This section outlines MEW's applications in such fields, focusing on how its process capabilities meet the specific needs of each field.

3.1. Energy Storage

MEW enables precise control over fibre porosity, diameter, and orientation, allowing for the creation of porous, multilayered architectures. Unlike conventional electrospinning, MEW avoids solvent residues, making it ideal for high-temperature processing.

Early applications in energy storage focused on polymer-based materials. In 2010, Cho et al. demonstrated MEW's potential by fabricating nanoscale polypropylene (PP) fibres with superhydrophobic properties, enhancing their suitability for battery separators, catalyst supports, and supercapacitor electrodes [51]. Based on this, Nayak et al. incorporated conductive agents, e.g., SO and NaCl into MEW fibres in 2012. As a result, they achieved

better electrical conductivity and chemical stability, which allows for wider applications in energy storage technologies [52].

More recently, the scope of MEW has expanded to include non-polymer materials, such as glass, valued for its exceptional thermal, optical, mechanical, and chemical properties. Before 2013, the direct production of submicron glass fibres would largely rely on mechanical stretching methods. In 2013, Praeger et al. used MEW to fabricate glass nanofibres and demonstrated its suitability for materials with high melting point and surface tension [53]. The resulting glass fibre scaffolds exhibited excellent mechanical strength and stability, ensuring reliable performance in demanding operational environments.

Despite these advancements, challenges remain in processing advanced energy materials (e.g., ZnO, MXene, and carbon-based materials), improving fibre conductivity, and reducing the high initial costs of equipment and processing. Future research should focus on enhancing thermal and electrical properties through surface coatings or the use of functional composites (e.g., PCL + graphene).

3.2. Filtration and Separation

MEW is widely used in the manufacture of porous membranes for air and water filtration. In 2018, Chala et al. developed a purple Tungsten oxide ($WO_{2.72}$)/PLA fibre membrane using MEW [54]. This membrane exhibited strong infrared absorption, which could accelerate light-driven water evaporation, and high hydrophobicity, which allows for floating on the water surface; hence, it was highly suitable for seawater desalination, water distillation, and salt production.

In terms of air filtration, Li et al. combined MEW with solution electrospinning (SES) technology in 2014 to make a composite PVA/PP membrane [55]. The PVA membrane was fabricated by SES, while the PP support layer was formed using MEW. In 2017, Shen et al. combined MEW with hot pressing equipment. By adjusting the diameter and arrangement of the fibres, they were able to produce fibre membranes with a filtration rate of more than 95% for particles greater than or equal to 2 μm [56]. Additionally, the membranes have high mechanical strength and can be used in the long term.

However, MEW's reliance on high-viscosity molten polymers limits its ability to produce nanoscale fibres, which are often required for high-precision filtration. Unlike SES, MEW does not benefit from solvent evaporation to achieve further shrinkage, and the melt jet must keep at a sufficient viscosity to avoid breakage. As a result, the fibre size is limited by the stable pulling process of the melt and achieving nanoscale becomes a challenge. Additionally, the electric field strength used in MEW is typically moderate, whereas nanoscale jets require highly uniform and intense fields for stable formation. Future research should be focussed on developing gradient membranes with variable porosity and fibre diameters to achieve more effective filtration and incorporating nanoparticles to create multifunctional membranes with antibacterial, photothermal, or selective separation capabilities.

3.3. Microfluidics

Microfluidics involves the manipulation of fluids within microscale structures (i.e., devices with dimensions less than 1 mm). At this scale, phenomena such as laminar flow, rapid diffusion, Dean flow, and efficient thermal transport become prominent due to the high surface-area-to-volume ratio. Traditional fabrication methods include soft lithography using polydimethylsiloxane (PDMS) and fused silica glass. However, MEW offers a promising alternative for creating microfluidic templates or directly forming microchannels, thanks to its ability to produce micro- and nanoscale fibres with high precision [57].

In 2018, Zeng et al. developed a simple and effective method for fabricating microfluidic channels based on MEW [58]. The process steps were (1) writing 2D or 3D PCL patterns

via MEW; (2) casting PDMS over the pattern; (3) peeling off the PDMS layer embedded with the sacrificial PCL material; and (4) bonding it to another PDMS layer by hot pressing. This approach enabled the creation of highly customizable microfluidic templates. In 2019, Kotz et al. expanded on this by using a similar sacrificial template method to fabricate hollow microstructures in fused silica glass with high precision and 3D design flexibility [59]. These structures incorporated conductive and biocompatible materials for applications in electrochemical sensing and bioanalysis.

Nonetheless, MEW faces similar limitations in microfluidics as in energy applications. The fabrication of highly intricate channels is constrained by fibre resolution, and interlayer adhesion between different materials must be optimised to ensure structural stability. Future directions include reducing nozzle diameters, increasing electric field strength, and incorporating stretchable materials like polyethylene oxide (PEO) to achieve more precise fibre control. Additionally, the integration of functional printing materials will enhance the stability and functionality of microfluidic devices.

3.4. Biomedical Scaffold

MEW enables the fabrication of micro- (1–1000 μm) and submicron-scale (100–1000 nm) fibres, allowing for the formation of highly porous structures with precise geometries. These characteristics make MEW particularly suitable for producing scaffolds that mimic the structures of native tissues such as cartilage, blood vessels, and tendons. Compared with scaffolds manufactured by other biomanufacturing techniques, MEW-based scaffolds exhibit superior mechanical strength and toughness. Furthermore, unlike solution electrospinning (SES), MEW does not require organic solvents, thereby eliminating potential toxic effects on sensitive cells and biomolecules.

3.4.1. MEW Scaffold Developments

In 2020, Paxton et al. used MEW technology to produce an expandable tubular scaffold [60]. The experiment successfully produced a five-layer structure with a diameter of 8 mm and a length of 48 mm. The scaffold showed excellent mechanical integrity and structural stability, highlighting its potential in the field of oesophageal and cardiovascular scaffolds.

In 2022, Diaz et al. introduced the dual-nozzle MEW technology for the first time [61], The experimental equipment is illustrated in Figure 11. Compared to traditional single-nozzle technology, the dual-nozzle configuration significantly enhances printing efficiency. It can also produce complex scaffolds with semi-woven properties. Diaz et al. used this technology to achieve high-precision fibre deposition, and the prepared scaffolds showed potential for biomedical applications. Table 6 provides an overview of other scaffolds made with MEW and their uses.

Table 6. Scaffolds fabricated by MEW.

Tissue	Scaffold Description	Ref.
Myocardial tissue	Hexagonal microstructure made by PCL	[62]
	Rectangular or square pore scaffold made by PHMGCL	[63]
Heart valve	Serpentine PCL architecture to mimic collagen fibres	[64]
Ligaments and tendons	Sinusoidal patterns of aligned, crimped collagen fibril imitation	[65]
Skin	PCL mixed with bioactive milk protein to promote cell growth and proliferation	[66]
Bone	PLA scaffolds with square pores	[67]
	PCL and chaotic gelatin scaffolds with square holes made by mixing MEW	[68]
	Calcium phosphate-coated PCL scaffolds with square pores and fibre offset	[69]

Table 6. *Cont.*

Tissue	Scaffold Description	Ref.
Cartilage	PLGA microspheres loaded with cells and PCL hybrid scaffolds with square pores	[70]
	Reinforced hyaluronic acid scaffold MEW PCL structures with square pores	[71]
Blood vessel	Tubular PCL scaffold with square pores with aortic root features	[72]
Periodontal tissue	PCL scaffolds with square pores with fluorinated calcium phosphate coating	[73]
Nerve tissue	Gold-coated PCL scaffold with square pores	[74]
	PCL scaffold with square pores and different surface modifications	[75]

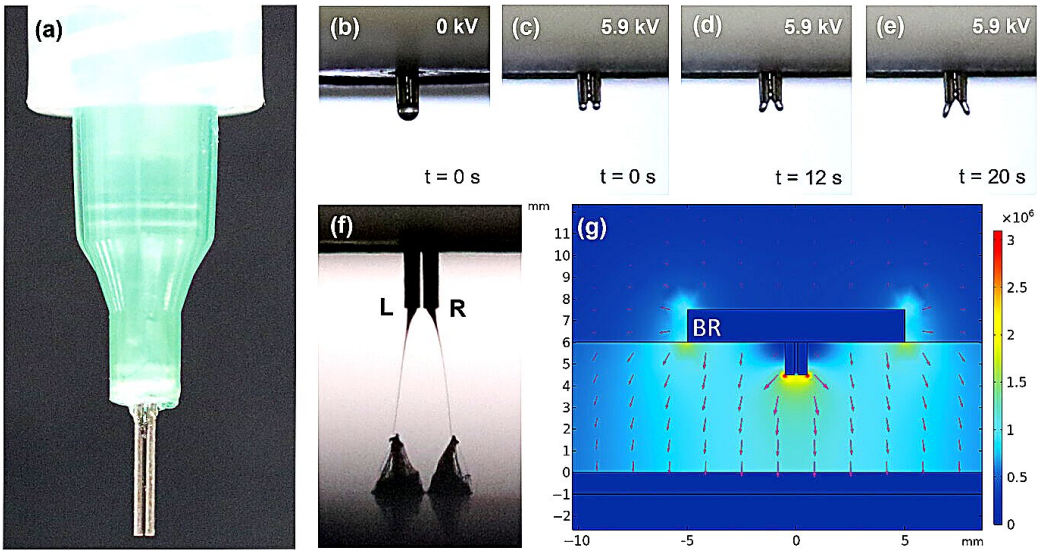

Figure 11. Dual-nozzle melt electrowriting system. (**a**) Modified 18G (initial diameter 0.838 mm) nozzle housing two 27G stainless steel nozzles (initial diameter 0.21mm), spaced 600 µm apart; (**b**) extrusion of molten polymer from the dual-nozzle setup without applied voltage; (**c**–**e**) sequence of molten polymer extrusion with applied voltage of 5.9 kV, which shows that the initial droplets which formed at the nozzles repel each other; (**f**) backlit image of the dual-nozzle system in operation, ejecting two distinct jets onto a stationary flat collector; (**g**) surface arrow plot showing the 2D electric field distribution within the MEW machine's dual-nozzle configuration (L: left nozzle, R: right nozzle, BR: brass ring) (Figure taken from [61]).

Despite these advancements, multi-nozzle MEW systems face several challenges, including electrostatic interference between nozzles, misalignment of fibre paths, and scalability limitations. To facilitate the transition of MEW from laboratory research to industrial-scale production, future efforts should focus on further developing electric field design and multi-layer fibre control strategy. These improvements will be crucial for unlocking MEW's full potential in tissue engineering and medical device manufacturing.

3.4.2. Hybrid Scaffold

Recent advancements in biomanufacturing have focused on integrating MEW with complementary fabrication techniques to improve process efficiency, enhance scaffold functionality, and enable the fabrication of more complex structures.

In 2015, Visser et al. introduced a method combining MEW-fabricated scaffolds with hydrogels to produce fibrous hydrogel composites [76]. Hydrogels are widely used in tissue engineering due to their highly hydrated, three-dimensional structure, which closely resembles the extracellular matrix (ECM). However, their mechanical properties are generally insufficient to meet the needs of the musculoskeletal system. By incorporating

MEW scaffolds, the mechanical strength of hydrogels can be significantly improved while keeping their biocompatibility.

In their study, Visser et al. first printed a 1 mm thick PCL scaffold using MEW. Gelatin methacrylamide (GelMA) and alginate hydrogels were then injected into the scaffold and crosslinked to form a composite structure. To evaluate performance, scaffolds with varying porosities were fabricated, and hydrogels were crosslinked using 12.5 mM and 25 mM ammonium persulfate/tetramethylethylenediamine (APS/TEMED). Compression and cyclic compression tests revealed that the composite scaffolds exhibited a stiffness up to 54 times greater than that of hydrogels alone, while maintaining biocompatibility of hydrogels and supporting high cell survival and matrix production. Additionally, MEW allows for precise control over scaffold geometry and porosity, enabling tailored designs for specific tissue engineering applications.

Despite these promising results, several challenges exist. Weak interfacial bonding between the hydrogel and scaffold may lead to delamination, and precise fibre network arrangement is difficult to control. Furthermore, mismatched degradation rates between the scaffold and hydrogel can compromise long-term stability. Addressing these issues will require further material innovation and process optimisation.

In 2019, Jungst et al. proposed a hybrid approach combining SES with MEW to fabricate vascular transplant scaffolds [77]. The two techniques have complementary advantages: SES produces randomly oriented nanofibre networks with high porosity, ideal for endothelial cell attachment and fibrosis, while MEW enables the fabrication of highly ordered micron-scale fibres suitable for guiding smooth muscle cell alignment and differentiation. The fabrication process is illustrated in Figure 12, followed by SEM imaging and pressure testing. After structural validation, cell seeding and culture were performed for biological analysis.

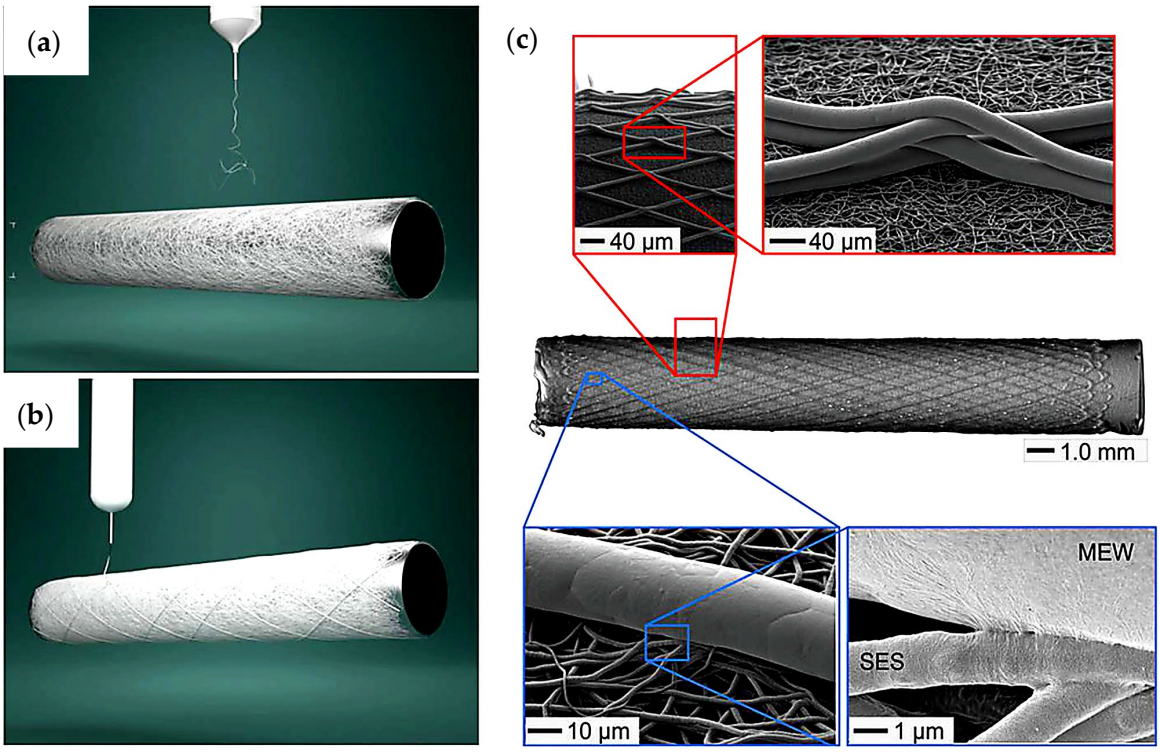

Figure 12. (**a**) The inner layer is fabricated using SES, (**b**) the outer layer is constructed by MEW, and (**c**) the scaffold is detached from the cylindrical collector. (Figure is taken from [77]).

This hybrid strategy results in a bilayer scaffold architecture that closely resembles native vascular tissue. The inner nanofibre layer supports endothelial cell growth, while the outer microfibre layer promotes smooth muscle cell organisation. The approach enhances both mechanical and biological performance and facilitates cell differentiation without the need for soluble biochemical cues or surface modifications.

3.5. Drug Delivery

MEW enables the fabrication of highly ordered, solvent-free, and porous microstructures, making it a promising technique for drug delivery applications. Drugs can be directly embedded within MEW fibres, coated onto structures fabricated by MEW, or integrated into composite systems such as hydrogel hybrids.

These approaches support sustained drug release and spatial delivery control while minimising solvent-induced cytotoxicity. MEW is primarily employed to create 3D scaffolds that promote cell growth in bioengineering. However, it is also used to precisely control the drug loading and release mechanisms. Although these two applications can be combined, their design goals and functional priorities differ.

In 2022, Xu et al. proposed a hybrid manufacturing approach combining MEW and melt electrospinning (MES) to produce reinforced nonwoven composite membranes [78]. The main difference between MEW and MES lies in the presence of the "whipping" phenomenon. When the nozzle speed is equal to or higher than critical translation speed (CTS), the jet forms a straight line, i.e., in the MEW mode. In contrast, MES occurs when the nozzle speed is much lower than CTS, resulting in randomly distributed fibres due to jet whipping near the collector.

In their method, MEW was used to print a regular PCL lattice, followed by MES deposition of drug-loaded PCL nonwoven fibres to form a composite scaffold. Solvent vapor annealing was applied to regulate PCL crystallinity, thereby adjusting the drug release rate. The resulting "shish-kebab"-like fibre structure was found to enhance drug release.

In 2023, Knierim et al. explored MEW for producing highly porous, drug-loaded amorphous solid dispersions (ASDs) for fast dissolving drug delivery systems [79]. By blending drugs with polymers during MEW, they fabricated microfibre scaffolds with high surface area, enabling rapid drug release. Table 7 presents more examples of MEW applications in drug delivery.

Despite its advantages, MEW faces several challenges: high processing temperatures that may degrade thermosensitive drugs, non-uniform drug distribution within composite materials, and the need to balance efficiency and consistency in large-scale production. Future research should focus on reducing processing temperatures using plasticisers to protect thermosensitive drugs, designing personalised drug-releasing scaffolds, and integrating MEW with complementary technologies to expand its clinical applicability [80].

Table 7. MEW in drug delivery.

Year	Description	Ref.
2017	Curcumin-loaded melt-electrospun PCL fibres with smoother surfaces and higher drug content	[81]
2017	PLA/starch/PCL/triclosan scaffolds with 3% nHAp to improve degradability, hydrophilicity, and antibacterial activity	[82]
2019	Fibrous membranes (fabricated by MEW) with varying ratios of PCL, PEG, and ciprofloxacin for wound dressing applications	[83]
2020	Portable melt electrospinning device designed to create PCL/Fe_3O_4 fibre membranes for magnetic hyperthermia therapy	[84]

4. Discussion

4.1. Challenges and Technological Limitations

4.1.1. System Design

One of the primary limitations of MEW lies in its system design, particularly regarding cost and accessibility. MEW setups require precise control over multiple processing parameters to regulate polymer melt flow, speed, scale, and accuracy. These demands result in complex, expensive, and often non-standard setups, which are typically assembled in-house within research laboratories. Such bespoke configurations hinder reproducibility and scalability. Unless cost-effective, standardised, and user-friendly systems become widely available, similar to the evolution of desktop 3D printers, MEW will likely remain limited to niche applications and mostly laboratory-scale use.

4.1.2. Material Limitation

MEW is constrained by a limited range of compatible materials, as it relies on polymers that can be precisely melt-extruded and electrospun at microscale resolution. Many commercially available polymers either fail to jet properly or degrade under the thermal and electrical conditions required for MEW. Additionally, variability in material behaviour from one batch to another affects process reliability and reproducibility. To improve adoption and industrial scalability, a wider selection of commercial polymers must be validated and optimised for MEW processing.

4.1.3. Scalability Constraints

Despite its precision in depositing micron and submicron fibres, MEW suffers from low throughput, limiting its scalability for industrial use. The process typically employs a single nozzle operating at low speeds to maintain resolution and structural accuracy. Scaling up with multi-nozzle systems introduces challenges such as electrical interference between jets. Moreover, increasing printing speed often compromises control over fibre deposition. These limitations make MEW unsuitable for large-scale or high-volume manufacturing.

4.1.4. Environmental Sensitivity

Environmental factors such as temperature, humidity, and airflow can have a significant impact on the MEW process. For example, humidity can alter the electrohydrodynamic behaviour of the polymer melt, affecting jet stability and fibre morphology. Similarly, ambient temperature variations can lead to inconsistent thermal gradients, which in turn affect fibre diameter as well as the deposition accuracy. Despite these sensitivities, most MEW studies neither mention nor report on the approaches used to manage the environment, making reproducibility difficult and complicating comparisons across laboratories.

4.1.5. Sustainability Considerations

Sustainability in MEW has not been fully explored, but it is an important consideration for future advancements in manufacturing. The process usually relies on specialty or medical-grade polymers that require excessive energy to produce and are typically non-biodegradable. In addition, MEW can be inefficient with resources due to trial-and-error optimisation, discarded prints, and low-volume production. Requirement of high temperatures and electric fields further contribute to its environmental footprint. Addressing these sustainability concerns is essential for expanding MEW's applicability in advanced manufacturing.

4.2. Future Direction

4.2.1. Hybrid Manufacturing

Advancements in MEW are expected to focus on hybrid manufacturing systems that integrate MEW with other technologies such as FFF, SES, and MES. These hybrid platforms will aim to improve production efficiency and address material compatibility challenges [9]. Additionally, multi-mode fibre manufacturing (where different fibre types are combined within a single structure) can yield complex, functional scaffolds that better mimic native tissue structures.

4.2.2. Material Innovation

The future development of MEW will depend on the creation of new thermoplastic and biodegradable polymers tailored to specific application needs in various fields [10]. In tissue engineering and bioengineering, materials with improved mechanical properties, biocompatibility, and suitability for long-term implants are particularly important [85]. Using conductive materials, such as metals, also presents new avenues and challenges for MEW manufacturing.

4.2.3. Improved Precision and Customisation

MEW's ability to produce fine, precisely controlled fibres is one of its main advantages. Further improvements in precision will be essential for applications requiring highly organised microstructures, such as neural scaffolds and microfluidic channels [85]. Although there are approximately 30 MEW publications on custom toolpath generation software (mostly developed in Python (available at: https://www.python.org) or MATLAB (available at https://matlab.mathworks.com)), only two have been publicly released [86]. Lacking widely used commercial software emphasises the need for advanced algorithms capable of generating complex 3D geometries.

4.2.4. Scale-Up

For the transition of MEW from laboratory research to industrial and clinical applications, scaling up is required. This includes automating the process, increasing printing speeds, and simplifying equipment design for ease of use. Such developments will play a crucial role, e.g., for producing patient-specific scaffolds in clinical surgery [10,83].

4.2.5. Environmental Control

Robust and reliable MEW processing requires systematic investigation to evaluate the impact of environmental effects and decide on the potential ways to control them. Establishing standard environmental measures and reporting practices will enhance reproducibility, consistency, and the translational potential of MEW research.

4.2.6. Sustainable Manufacturing

As the manufacturing sector moves toward circular and sustainable practices, MEW must adapt by incorporating bio-based, recyclable, or reusable feedstocks. Life cycle assessments and closed-loop material systems (where materials are continuously recovered and reused) can minimise waste and reduce reliance on virgin resources. Developing customised blends of recycled polymers with engineered flow and deformation properties (through additives or processing) will provide a viable, environmentally friendly approach for microscale manufacturing using MEW process.

5. Conclusions

Melt electrowriting (MEW) is a promising additive manufacturing technology that is unique in its ability to produce highly ordered microscale fibre structures with extremely high precision. This review provided a detailed overview of the modelling approaches for the four key stages of MEW (heating and extrusion, Taylor cone formation, melt jet formation, and fibre deposition). Additionally, the practical applications of MEW in diverse fields, including energy storage, filtration, microfluidics, biomedical engineering, and drug delivery, were discussed.

Significant progress has been made in developing computational models that enhance understanding and simulation of the MEW process. These models cover all aspects of MEW, from Taylor cone formation to fibre collection, while also enabling control over key parameters such as voltage, temperature, and extrusion rate. Such models allow for improved prediction and control of fibre diameter and deposition accuracy and help address common defects such as jet instability, fibre pulsation, and breakage.

MEW has a wide range of applications, especially in the field of bioengineering. It enables the fabrication of biomimetic scaffolds with tunable porosity and geometry, which is essential for cell growth and tissue regeneration. In drug delivery and microfluidics, MEW facilitates solvent-free, structurally precise construction, addressing challenges in controlled release and miniaturisation. Moreover, the application of MEW in energy and filtration systems highlights its versatility in functional materials engineering.

Despite these advantages, MEW faces several limitations. These include difficulties in producing nanoscale fibres, limited scalability for industrial applications, and compatibility issues with advanced materials such as conductive polymers and metals. Additionally, environmental conditions can significantly influence process reliability and repeatability yet are often overlooked in experimental setups. Existing models usually rely on simplifying assumptions, e.g., uniform temperature and Newtonian fluid behaviour, which limit their accuracy in simulating real-life cases.

Future research should focus on the following three directions: (1) developing more accurate physical models to account for non-Newtonian rheology, electrohydrodynamic instabilities, and environmental effects; (2) integrating machine learning and closed-loop control systems to improve printing accuracy, repeatability, and automation; and (3) expanding MEW-compatible materials to include bioactive, electrically conductive, and biodegradable polymers. In addition, process innovations in nozzle design and hybrid manufacturing are crucial for translating MEW from laboratory environments to scalable, practical applications. The environmental control and sustainability of MEW should also be given attention.

Author Contributions: Conceptualisation, H.J. and Z.M.K.; methodology, H.J.; resources, Z.M.K.; writing—original draft preparation, H.J.; writing—review and editing, H.J., W.M., W.W., and Z.M.K.; supervision, W.M. and Z.M.K. All authors have read and agreed to the published version of the manuscript.

Funding: This research received no external funding.

Data Availability Statement: No new data were created or analysed in this study. Data sharing is not applicable to this article.

Conflicts of Interest: The authors declare no conflicts of interest.

References

1. Liu, J.; Wen, P. Metal vaporization and its influence during laser powder bed fusion process. *Mater. Des.* **2022**, *215*, 110505. [CrossRef]
2. Sieminski, P. Chapter 7—Introduction to fused deposition modelling. In *Additive Manufacturing*; Elsevier: Amsterdam, The Netherlands, 2021; pp. 217–275. [CrossRef]
3. Penumakala, P.K.; Santo, J.; Thomas, A. A critical review on the fused deposition modelling of thermoplastic polymer composites. *Compos. Part. B Eng.* **2020**, *201*, 108336. [CrossRef]
4. Nollet, A.; Stack, T. On electricity communicated by sparks. *Philos. Trans. R. Soc. Lond.* **1753**, *45*, 187.
5. Cooley, J.F. Improved Methods of and Apparatus for Electrically Separating the Relatively Volatile Liquid Component from the Component of Relatively Fixed Substances of Composite Fluids. United Kingdom Patent 6385, 19 May 1900.
6. Boland, E.D.; Wnek, G.E.; Simpson, D.G.; Pawlowski, K.J.; Bowlin, G.L. Tailoring tissue engineering scaffolds using electrostatic processing techniques: A study of poly(glycolic acid) electrospinning. *J. Macromol. Sci. Part. A* **2001**, *38*, 1231–1243. [CrossRef]
7. Pham, Q.P.; Sharma, U.; Mikos, A.G. Electrospun poly(epsilon-caprolactone) microfiber and multilayer nanofiber/microfiber scaffolds: Characterization of scaffolds and measurement of cellular infiltration. *Biomacromolecules* **2006**, *7*, 2796–2805. [CrossRef]
8. Viswanathan, G.; Murugesan, S.; Pushparaj, V.; Nalamasu, O.; Ajayan, P.M.; Linhardty, R.J. Preparation of biopolymer fibers by electrospinning from room temperature ionic liquids. *Biomacromolecules* **2006**, *7*, 415–418. [CrossRef]
9. Loewner, S.; Heene, S.; Baroth, T.; Heymann, H.; Cholewa, F.; Blume, H.; Blume, C. Recent advances in melt electro writing for tissue engineering for 3D printing of microporous scaffolds for tissue engineering. *Front. Bioeng. Biotechnol.* **2022**, *10*, 896719. [CrossRef]
10. Dalton, P.D. Melt electrowriting with additive manufacturing principles. *Curr. Opin. Biomed. Eng.* **2017**, *2*, 49–57. [CrossRef]
11. Brown, T.D.; Dalton, P.D.; Hutmacher, D.W. Direct writing by way of melt electrospinning. *Adv. Mater.* **2011**, *21*, 5651–5657. [CrossRef]
12. Shahverdi, M.; Seifi, S.; Akbari, A.; Mohammadi, K.; Shamloo, A.; Movahhedy, M.R. Melt electrowriting of PLA, PCL, and composite PLA/PCL scaffolds for tissue engineering application. *Sci. Rep.* **2022**, *12*, 19935. [CrossRef]
13. Eichholz, K.F.; Gonçalves, I.; Barceló, X.; Federici, A.S.; Hoey, D.A.; Kelly, D.J. How to design, develop and build a fully-integrated melt electrowriting 3D printer. *Addit. Manuf.* **2022**, *58*, 102998. [CrossRef]
14. *ASTM52900-15*; Additive Manufacturing—General Principles—Terminology. ASTM International: West Conshohocken, PA, USA, 2015.
15. Altıparmak, S.C.; Yardley, V.A.; Shi, Z.; Lin, J. Extrusion-based additive manufacturing technologies: State of the art and future perspectives. *J. Manuf. Process.* **2022**, *83*, 607–636. [CrossRef]
16. Altıparmak, S.C.; Daminabo, S.I.C. Suitability analysis for extrusion-based additive manufacturing process. *Addit. Manuf. Front.* **2024**, *3*, 200106. [CrossRef]
17. Bellini, A. Fused Deposition of Ceramics: A Comprehensive Experimental, Analytical and Computational Study of Material Behaviour, Fabrication Process and Equipment Design. Ph.D. Thesis, Drexel University Philadelphia, Philadelphia, PA, USA, 2002. Available online: https://www.proquest.com/openview/7a42ce9237bce7b25bee6dc952e70efb/1?pq-origsite=gscholarandcbl=18750anddiss=y (accessed on 6 May 2025).
18. Ramanath, H.S.; Chua, C.K.; Leong, K.F. Melt flow behaviour of poly-ε-caprolactone in fused deposition modelling. *J. Mater. Sci: Mater. Med.* **2008**, *19*, 2541–2550. [CrossRef]
19. Monzón, M.D.; Gibson, I.; Benítez, A.N. Process and material behaviour modelling for a new design of micro-additive fused deposition. *Int. J. Adv. Manuf. Technol.* **2013**, *67*, 2717–2726. [CrossRef]
20. Ortega, Z.; Alemán, M.E.; Benítez, A.N.; Monzon, M.D. Theoretical-experimental evaluation of different biomaterials for parts obtaining by fused deposition modelling. *Meas. J. Int. Meas. Confed.* **2016**, *89*, 137–144. [CrossRef]
21. Shaqour, B.; Abuabiah, M.; Abdel-Fattah, S. Gaining a better understanding of the extrusion process in fused filament fabrication 3D printing: A review. *Int. J. Adv. Manuf. Technol.* **2021**, *114*, 1279–1291. [CrossRef]
22. Bellini, A.; Guceri, S.; Bertoldi, M. Liquefier dynamics in fused deposition. *ASME J. Manuf. Sci. Eng.* **2004**, *126*, 237–246. [CrossRef]
23. Osswald, T.A.; Puentes, J.; Kattinger, J. Fused filament fabrication melting model. *Addit. Manuf.* **2018**, *22*, 51–59. [CrossRef]
24. Taylor, G.I. Disintegration of water drops in an electric field. *Proc. R. Soc. Lond.* **1964**, *280*, 383–397. [CrossRef]
25. Taylor, G.I. Electrically driven jets. *Proc. R. Soc. Lond.* **1969**, *313*, 453–475. [CrossRef]
26. Marginean, I.; Parvin, L.; Heffernan, L.; Vertes, A. Flexing the electrified meniscus: The birth of jet in electrosprays. *Anal. Chem.* **2004**, *76*, 4202–4207. [CrossRef]
27. Melcher, J.; Taylor, G.I. Electrohydrodynamics: A review of the role of interfacial shear stresses. *Annu. Rev. Fluid. Mech.* **1969**, *1*, 111–146. [CrossRef]
28. Pan, Y.; Zeng, L. Simulation and validation of droplet generation process for revealing three design constraints in electrohydrodynamic jet printing. *Micromachines* **2019**, *10*, 94. [CrossRef]

29. Gañán-Calvo, A.; Dávila, J.; Barrero, A. Current and droplet size in the electrospraying of liquids. Scaling laws. *J. Aerosol Sci.* **1997**, *28*, 249–275. [CrossRef]
30. Barrero, A.; Gañán-Calvo, A.; Dávila, J.; Palacios, A.; Gómez-González, E. The role of the electrical conductivity and viscosity on the motions inside taylor cones. *J. Electrost.* **1999**, *47*, 13–26. [CrossRef]
31. Yan, F.; Farouk, B.; Ko, F. Numerical modeling of an electrostatically driven liquid meniscus in the cone–jet mode. *J. Aerosol Sci.* **2003**, *34*, 99–116. [CrossRef]
32. Lastow, O.; Balachandran, W. Numerical simulation of electrohydrodynamic (EHD) atomization. *J. Electrost.* **2006**, *64*, 850–859. [CrossRef]
33. Wu, X.; Oleshuk, R.D.; Cann, N.M. Characterization of microstructured fibre emitters: In pursuit of improved nano electrospray ionization performance. *Analyst* **2012**, *137*, 4150–4161. [CrossRef]
34. Sachin, K. Singh and Arunkumar Subramanian. Phase-field simulations of electrohydrodynamic jetting for printing nano-to-microscopic constructs. *RSC Adv.* **2020**, *10*, 25022–25028. Available online: https://pubs.rsc.org/en/content/articlelanding/2020/ra/d0ra04214e#!divAbstract (accessed on 20 January 2025).
35. Cândido, S.; Páscoa, J.C. A three-dimensional numerical investigation of taylor cone jets instabilities using VOF method. In Proceedings of the ASME 2023 International Mechanical Engineering Congress and Exposition, New York, NY, USA, 29 October–2 November 2023; Volume 9: Fluids Engineering. [CrossRef]
36. Non-Newtonian Fluid. Available online: https://en.wikipedia.org/wiki/Non-Newtonian_fluid (accessed on 10 May 2025).
37. Spivak, A.; Dzenis, Y.; Reneker, D. A model of steady state jet in the electrospinning process. *Mech. Res. Commun.* **2000**, *27*, 37–42. [CrossRef]
38. Hohman, M.M.; Shin, M.; Rutledge, G.; Brenner, M.P. Electrospinning and electrically forced jets. I. Stability theory. *Phys. Fluids* **2001**, *13*, 2201–2220. [CrossRef]
39. Hohman, M.M.; Shin, M.; Rutledge, G.; Brenner, M.P. Electrospinning and electrically forced jets. II. Applications. *Phys. Fluids* **2001**, *13*, 2221–2236. [CrossRef]
40. Feng, J.J. The stretching of an electrified non-Newtonian jet: A model for electrospinning. *Phys. Fluids* **2002**, *14*, 3912–3926. [CrossRef]
41. Vlassopoulos, D.; Hatzikiriakos, S.G. A generalized Giesekus constitutive model with retardation time and its association to the spurt effect. *J. Non-Newton. Fluid. Mech.* **1995**, *57*, 119–136. [CrossRef]
42. Carroll, C.P.; Joo, Y.L. Electrospinning of viscoelastic Boger fluids: Modelling and experiments. *Phys. Fluids* **2006**, *18*, 053102. [CrossRef]
43. Zhmayev, E.; Zhou, H.; Joo, Y.L. Modelling of non-isothermal polymer jets in melt electrospinning. *J. Non-Newton. Fluid. Mech.* **2008**, *153*, 95–108. [CrossRef]
44. Zhmayev, E.; Cho, D.; Joo, Y.L. Modelling of melt electrospinning for semi-crystalline polymers. *Polymer* **2010**, *51*, 274–290. [CrossRef]
45. Nakamura, K.; Katayama, K.; Amano, T. Some aspects of nonisothermal crystallization of polymers. II. Consideration of the isokinetic condition. *J. Appl. Polym. Sci.* **1973**, *17*, 1031–1041. [CrossRef]
46. Mayadeo, N.; Morikawa, K.; Naraghi, M.; Green, M.J. Modelling of downstream heating in melt electrospinning of polymers. *J. Polym. Sci. Part. B Polym. Phys.* **2017**, *55*, 1393–1405. [CrossRef]
47. Hrynevich, A.; Liashenko, I.; Dalton, P.D. Accurate prediction of melt electrowritten laydown patterns from simple geometrical considerations. *Adv. Mater. Technol.* **2020**, *5*, 2000772. [CrossRef]
48. Cao, K.; Zhang, F.; Wang, B.; Sun, Y.; Zaeri, A.; Zgeib, R.; Mansouri, M.; Chang, R.C. Analytical interpretation of microscale fiber deviation in designing for polymer melt electrohydrodynamic-based additive manufacturing. *Addit. Manuf.* **2022**, *58*, 103035. [CrossRef]
49. Cao, K.; Zhang, F.; Zaeri, A.; Zgeib, R.; Chang, R.C. A holistic model for melt electrowritten three-dimensional structured materials based on residual charge. *Int. J. Bioprint.* **2022**, *9*, 656. [CrossRef] [PubMed]
50. Ko, J.; Bhullar, S.K.; Mohtaram, N.K.; Willerth, S.M.; Jun, M.B.G. Using mathematical modelling to control topographical properties of poly(ε-caprolactone) melt electrospun scaffolds. *J. Micromech. Microeng.* **2014**, *24*, 065009. [CrossRef]
51. Cho, D.; Zhou, H.; Cho, Y.; Audus, D.; Joo, Y.L. Structural properties and superhydrophobicity of electrospun polypropylene fibers from solution and melt. *Polymer* **2010**, *51*, 6005–6012. [CrossRef]
52. Nayak, R.; Kyratzis, I.L.; Truong, Y.B.; Padhye, R.; Arnold, L. Melt-electrospinning of polypropylene with conductive additives. *J. Mater. Sci.* **2012**, *47*, 6387–6396. [CrossRef]
53. Praeger, M.; Saleh, E.; Vaughan, A.; Stewart, W.J.; Loh, W.H. Fabrication of nanoscale glass fibers by electrospinning. *Appl. Phys. Lett.* **2012**, *100*, 063114. [CrossRef]
54. Chala, T.F.; Wu, C.M.; Chou, M.H.; Guo, Z.L. Melt electrospun reduced tungsten oxide/polylactic acid fiber membranes as a photothermal material for light-driven interfacial water evaporation. *ACS Appl. Mater. Interfaces* **2018**, *10*, 28955–28962. [CrossRef]

55. Li, X.; Yang, W.; Li, H.; Wang, Y.; Bubakir, M.M.; Ding, Y.; Zhang, Y. Water filtration properties of novel composite membranes combining solution electrospinning and needleless melt electrospinning methods. *J. Appl. Polym. Sci.* **2015**, *132*. [CrossRef]
56. Shen, Y.; Xia, S.; Yao, P.; Gong, R.H.; Liu, Q.; Deng, B. Structure regulation and properties of melt-electrospinning composite filter materials. *Fibers Polym.* **2017**, *18*, 1568–1579. [CrossRef]
57. Gale, B.; Jafek, A.; Lambert, C.; Goenner, B.; Moghimifam, H.; Nze, U.; Kamarapu, S. A review of current methods in microfluidic device fabrication and future commercialization prospects. *Inventions* **2018**, *3*, 60. [CrossRef]
58. Zeng, J.; Wang, H.; Lin, Y.; Zhang, J.; Liang, F.; Fang, F.; Yang, F.; Wang, P.; Zhu, Z.; Chen, X. Fabrication of microfluidic channels based on melt-electrospinning direct writing. *Microfluid. Nanofluid.* **2018**, *22*, 23. [CrossRef]
59. Kotz, F.; Risch, P.; Arnold, K.; Sevim, S.; Puigmartí-Luis, J.; Quick, A.; Thiel, M.; Hrynevich, A.; Dalton, P.D.; Helmer, D.; et al. Fabrication of arbitrary three-dimensional suspended hollow microstructures in transparent fused silica glass. *Nat. Commun.* **2019**, *10*. [CrossRef]
60. Paxton, N.C.; Daley, R.; Forrestal, D.P.; Allenby, M.C.; Woodruff, M.A. Auxetic tubular scaffolds via melt electrowriting. *Mater. Des.* **2020**, *193*, 108787. [CrossRef]
61. Diaz, R.S.; De-Juan-Pardo, E.M.; Dalton, P.D.; Dargaville, T.R. Semi-woven structures via dual nozzle melt electrowriting. *Macromol. Mater. Eng.* **2023**, *308*, 2200526. [CrossRef]
62. Castilho, M.; Maher, M.G.; Metz, C.H.; Hochleitner, G.; Groll, J.; Doevendans, P.A.; Ito, K.; Sluijter, J.P.G.; Malda, J. Melt electrowriting allows tailored microstructural and mechanical design of scaffolds to advance functional human myocardial tissue formation. *Adv. Funct. Mater.* **2018**, *28*, 1803151. [CrossRef]
63. Castilho, M.; Feyen, D.; Flandes-Iparraguirre, M.; Hochleitner, G.; Groll, J.; Doevendans, P.A.F.; Vermonden, T.; Ito, K.; Sluijter, J.P.G.; Malda, J. Melt electrospinning writing of poly-hydroxymethylglycolide-co-ε-caprolactone-based scaffolds for cardiac tissue engineering. *Adv. Healthc. Mater.* **2017**, *6*, 1700311. [CrossRef] [PubMed]
64. Saidy, N.T.; Wolf, F.; Bas, O.; Keijdener, H.; Hutmacher, D.W.; Mela, P.; De-Juan-Pardo, E.M. Biologically inspired scaffolds for heart valve tissue engineering via melt electrowriting. *Small* **2019**, *15*, 1900873. [CrossRef]
65. Hochleitner, G.; Chen, F.; Blum, C.; Dalton, P.D.; Amsden, B.; Groll, J. Melt electrowriting below the critical translation speed to fabricate crimped elastomer scaffolds with non-linear extension behaviour mimicking that of ligaments and tendons. *Acta Biomater.* **2018**, *72*, 110–120. [CrossRef]
66. Hewitt, E.; Mros, S.; McConnell, M.; Cabral, J.D.; Ali, A. Melt-electrowriting with novel milk protein/PCL biomaterials for skin regeneration. *Biomed. Mater.* **2019**, *14*, 055013. [CrossRef]
67. Meng, J.; Boschetto, F.; Yagi, S.; Marin, E.; Adachi, T.; Chen, X.; Pezzotti, G.; Sakurai, S.; Yamane, H.; Xu, H. Design and manufacturing of 3D high-precision micro-fibrous poly(L-lactic acid) scaffold using melt electrowriting technique for bone tissue engineering. *Mater. Des.* **2021**, *210*, 110063. [CrossRef]
68. Wang, Z.; Wang, H.; Xiong, J.; Li, J.; Miao, X.; Lan, X.; Liu, X.; Wang, W.; Cai, N.; Tang, Y. Fabrication and in vitro evaluation of PCL/gelatin hierarchical scaffolds based on melt electrospinning writing and solution electrospinning for bone regeneration. *Mater. Sci. Eng. C* **2021**, *128*, 112287. [CrossRef]
69. Abbasi, N.; Lee, R.S.B.; Ivanovski, S.; Love, R.M.; Hamlet, S. In vivo bone regeneration assessment of offset and gradient melt electrowritten (MEW) PCL scaffolds. *Biomater. Res.* **2020**, *24*, 17. [CrossRef]
70. Han, Y.; Lian, M.; Sun, B.; Jia, B.; Wu, Q.; Qiao, Z.; Dai, K. Preparation of high precision multilayer scaffolds based on Melt Electro-Writing to repair cartilage injury. *Theranostics* **2020**, *10*, 10214–10230. [CrossRef]
71. Galarraga, J.H.; Locke, R.C.; Witherel, C.E.; Stoeckl, B.D.; Castilho, M.; Mauck, R.L.; Malda, J.; Levato, R.; Burdick, J.A. Fabrication of MSC-laden composites of hyaluronic acid hydrogels reinforced with MEW scaffolds for cartilage repair. *Biofabrication* **2021**, *14*, 014106. [CrossRef] [PubMed]
72. Saidy, N.T.; Shabab, T.; Bas, O.; Menne, M.; Henry, T.; Hutmacher, D.W.; Mela, P. Melt electrowriting of complex 3D anatomically relevant scaffolds. *Front. Bioeng. Biotechnol.* **2020**, *8*, 550778. [CrossRef] [PubMed]
73. Daghrery, A.; Ferreira, J.A.; Araújo, S.; Clarkson, B.H.; Eckert, G.J.; Bhaduri, S.B.; Malda, J.; Bottino, M.C. A highly ordered, nanostructured fluorinated CaP-coated melt electrowritten scaffold for periodontal tissue regeneration. *Adv. Healthc. Mater.* **2021**, *10*, 2101152. [CrossRef] [PubMed]
74. Wang, Y.; Zhang, Y.; Zhang, Z.; Su, Y.; Wang, Z.; Dong, M.; Chen, M. An injectable high-conductive bimaterial scaffold for neural stimulation. *Colloids Surf. B Biointerfaces.* **2020**, *195*, 111210. [CrossRef]
75. Chen, T.; Jiang, H.; Zhu, Y.; Chen, X.; Zhang, D.; Li, X.; Shen, F.; Xia, H.; Min, Y.; Xie, K. Highly ordered 3D tissue engineering scaffolds as a versatile culture platform for nerve cells growth. *Macromol. Biosci.* **2021**, *21*, 2100047. [CrossRef]
76. Visser, J.; Melchels, F.P.; Jeon, J.E.; Van Bussel, E.M.; Kimpton, L.S.; Byrne, H.M.; Dhert, W.J.; Dalton, P.D.; Hutmacher, D.W.; Malda, J. Reinforcement of hydrogels using three-dimensionally printed microfibres. *Nat. Commun.* **2015**, *6*, 6933. [CrossRef]
77. Jungst, T.; Pennings, I.; Schmitz, M.; Rosenberg, J.W.P.; Groll, J.; Gawlitta, D. Heterotypic scaffold design orchestrates primary cell organization and phenotypes in cocultured small diameter vascular grafts. *Adv. Funct. Mater.* **2019**, *29*, 1905987. [CrossRef]

78. Xu, T.; Gu, J.; Meng, J.; Du, L.; Kumar, A.; Xu, H. Melt electrowriting reinforced composite membrane for controlled drug release. *J. Mech. Behav. Biomed. Mater.* **2022**, *132*, 105277. [CrossRef]
79. Keßler, L.; Mirzaei, Z.; Kade, J.C.; Luxenhofer, R. Highly porous and drug-loaded amorphous solid dispersion microfiber scaffolds of indomethacin prepared by melt electrowriting. *ACS Appl. Polym. Mater.* **2023**, *5*, 913–922. [CrossRef]
80. Lama-Odría, M.; Valle, L.J.; Puiggalí, J. *Melt Electrospinning and Electrowriting for Pharmaceutical and Biomedical Applications*; Springer: Berlin/Heidelberg, Germany, 2023; Volume 2. [CrossRef]
81. Lian, H.; Meng, Z. Melt electrospinning vs. solution electrospinning: A comparative study of drug-loaded poly(ε-caprolactone) fibres. *Mater. Sci. Eng. C* **2017**, *74*, 117–123. [CrossRef] [PubMed]
82. Davachi, S.M.; Shiroud, H.B.; Hejazi, I.; Seyfi, J.; Oliaei, E.; Farzaneh, A.; Rashedi, H. Interface modified polylactic acid/starch/poly ε-caprolactone antibacterial nanocomposite blends for medical applications. *Carbohydr. Polym.* **2017**, *155*, 336–344. [CrossRef] [PubMed]
83. He, L.; Deng, X.; Zhou, Q.; Zhang, D.; Liu, L.; Ye, J.; Yin, C. Controlled release of antibiotics from poly-ε-caprolactone/polyethylene glycol wound dressing fabricated by direct-writing melt electrospinning. *Polym. Adv. Technol.* **2019**, *30*, 425–434. [CrossRef]
84. Hu, P.; Zhao, Y.; Zhang, J.; Yu, S.; Yan, J.; Wang, X.; Hu, M.; Xiang, H.; Long, Y. In situ melt electrospun polycaprolactone/Fe_3O_4 nanofibers for magnetic hyperthermia. *Mater. Sci. Eng. C* **2020**, *110*, 110708. [CrossRef]
85. Afghah, F.; Dikyol, C.; Altunbek, M.; Koc, B. Biomimicry in bio-manufacturing: Developments in melt electrospinning writing technology towards hybrid biomanufacturing. *Appl. Sci.* **2019**, *9*, 3540. [CrossRef]
86. Devlin, B.L.; Kuba, S.; Hall, P.C.; McCosker, A.B.; Pickering, E.; Dalton, P.D.; Klein, T.J.; Woodruff, M.A.; Paxton, N.C. A melt electrowriting toolbox for automated G-code generation and toolpath correction of flat and tubular constructs. *Adv. Mater. Technol.* **2024**, *9*, 2400419. [CrossRef]